

ABSTRACT

In this thesis we give an accurate and general model that can be used to predict short-range/time UWB reflection. This reflection occurs when the source and the receiver are near a single reflecting boundary. Our approach uses an image-based method based on Laplace-transform formulation of the Sommerfeld half-space problem. The boundary between two mediums is replaced by a point source of given strength and location. The component amplitude of the image is chosen such that transverse electric and magnetic fields are continuous across the boundary. The complete field formulation is based on a simple branch-integral consisted in the reflection coefficient. Since the analysis is done in the frequency domain, UWB pulse is recovered by an inverse of Fourier transform.

TABLE OF CONTENTS

LIST OF FIGURES	vii
LIST OF SYMBOLS	x
Chapter 1 INTRODUCTION	1
1.1 Introduction	1
1.2 Background	5
1.3 Problem Statement and Objectives	10
Chapter 2 BASIC PRINCIPLES OF MODULATION AND DEMODULATION	12
2.1 Introduction	12
2.2 Pulse Position Modulation	13
2.3 Matched Filter Demodulation	23
Chapter 3 SPHERICAL WAVE REFLECTION FROM A PLANAR INTERFACE	36
3.1 Introduction	36
3.2 Free Space Propagation	38
3.3 Parallel Polarization	42
3.4 Perpendicular Polarization	48
3.5 Inverse Laplace Transform of the Reflection Coefficient	53
3.6 Radiated Field	63
Chapter 4 INFLUENCE OF THE SHORT-TIME/RANGE REFLECTION ON THE UWB SIGNAL	74
4.1 Introduction	74
4.2 Time-domain Solution	75
4.3 Relationship Between Hertzian Potential and Electric Field	81

4.4 Implementation of the Model	84
Chapter 5 CONCLUSIONS	91
Appendix A DETAILED DERIVATION OF THE ENTIRE FIELD	94
REFERENCES	101
BIOGRAPHY	103

Chapter 1

INTRODUCTION

1.1 Introduction

Ultra wideband (UWB) radio signals are comprised of sub-nanosecond duration electromagnetic pulses. A sequence of pulses is used to encode a transmitted symbol. The technology used to generate, transmit and receive UWB signals was developed in the early 1960's. UWB is also referred to as baseband, impulse or carrier-free radio because it is characterized by extremely short duration and low energy impulses which are transmitted over a wide range of frequencies without using a dedicated carrier frequency. UWB's high data bandwidth and frequency diversity make it suitable for high-speed data communication in indoor environments, where multipath fading is likely.

UWB is a relatively new term, however, the UWB radio is not a new concept. At the end of 19th century and the beginning of 20th century the only known radio technology was pulse radio. Heinrich Hertz used a pulsed spark discharge to generate electromagnetic waves before sinusoidal carriers were used^[1]. However, only recently has UWB become competitive technology in wireless communication after its pioneers Louis de Rosa, Conrad Hoepfner, Gerald Ross, and Henning

Harmuth, made it possible to efficiently generate and control UWB signals and apply modulation, coding, and multiple access techniques.

In early 1940's, Louis de Rosa, filed for two patents on the "radio detection systems in which the transmission of impulses may occur either steadily or at random" and "random impulse system"^[2] ^[3]. In the first patent he proposed a solution for the transmission of high voltage pulses and detection of echoes caused by the presence of obstacles within the range of the system. In his second patent he provided a method of generating a series of pulses occurring at random time intervals. When used as a modulation method, it greatly minimized the possibility of jamming. It was not until long after the World War II that he received these patents. Many patents at this time were put on hold because US government thought they contained valuable wartime secrets.

Similarly, Conrad Hoepfner received a patent in 1961 that outlined a pulse communication system meant to reduce interference and jamming, and to enhance specificity, reliability, and secrecy^[4]. Gerald Ross and Henning Harmuth are responsible for modern contributions to UWB technology. In 1960's they both published papers incorporating the now 50-year-old concept of matched filtering and they applied it into UWB systems. Ross and Harmuth's research focused on the study of main components of UWB transmission, pulse generation, and pulse detection. Ross did his PhD dissertation in time-domain electromagnetics where he

described transient behavior of microwave networks through their impulse response^[5]. A portion of his thesis was published in a paper in 1966^[6], and also filed for his first patent where he outlined the design of a pulse generator^[7]. Ross had many patents, however, his 1973 patent pioneered the usage of UWB in communications^[8]. Harmuth's interest started off through implementation of Walsh function in communications^{[9] [10]} and resulted in many different designs for transmitters and receivers, such as transmitters and receivers using nonsinusoidal carriers^[11], and high-resolution radar for pulse durations of $1ns$ and spread-spectrum transmission^[12]. Since the basic designs for UWB systems appeared in 1970's, the only improvement in UWB technology occurred in design of different subsystems, but not in the system concepts themselves.

Due to its unique properties, UWB has already found its place in many different wireless applications. One of the most significant features of UWB technology is security. The interception of randomly spaced narrow pulses is extremely difficult. Due to this reason, UWB system can accommodate large number of users in multipath environment. Since 1970's, UWB systems have been successfully used in the ground, and wall penetration, position location, collision warning for avoidance, fluid level detection, intruder detection, and vehicle radar measurements. Newer applications are more focused on indoor wireless, like small local area networks, wireless broadcast of high definition television (HDTV), and

through-wall imaging system to detect the movement of people behind walls. UWB and its application to short-range personal area networking (PAN) is currently being explored. UWB systems are capable of transmitting data 100 times faster than Bluetooth's speed of 1 Ms/s^[13]. This also makes UWB suitable for connecting devices like camcorders, TVs, computers, and peripherals.

The many advantages that UWB technology has over other wireless technologies has created commercial interest. However, UWB signals overlay large parts of the radio spectrum. The UWB signal might disrupt a host of wireless applications. National Telecommunications Information Administration showed that UWB signals could make it more difficult for GPS receivers to lock onto satellite signals, and could also reduce their accuracy. Possible harmful interference of UWB signals to narrowband receivers and transmitters are not completely understood either from analytical or experimental point of view. In the case of more than one UWB communication system operating in asynchronous mode, the assumed non-appearance of interference has yet to be validated. In the multipath environment pulses that reach the receiver in or out of phase with the original signal will interfere with reception to a greater or lesser extent.

The commercial use of UWB has been allowed, however, the Federal Communications Commission (FCC) has to put strict limits on the new technology. Consumer UWB radios are limited to operate with their -10 dB bandwidths in the

frequency ranges: below 960MHz, between 3.1 and 10.6 GHz, and between 22 and 29 GHz. However, FCC is still amending the rules concerned with who operates certain applications and for what purposes^[14]. For instance, through-wall imaging systems are allowed for law enforcement, emergency rescue, and firefighter personnel in emergency situations in limited bands below 960MHz and above 3.1 GHz. In other words, new radios could be limited in the either distance they can transmit or the data rates that they can achieve^[15]. Before FCC restrictions, UWB used the full bandwidth, which maximized capacity and at the same time minimized the amount of energy in any given frequency band. Sending information in pulses required relatively simple design, and therefore such systems are cheaper than conventional radio structures. Conventional narrowband radios require components that will limit the frequencies they are allowed to use. FCC frequency restrictions on UWB signal might add cost to new commercial products.

In our work, the reflection of an UWB pulse from a planar dielectric surface will be analyzed. To this end an exact image formulation will be presented and its predictions evaluated. This work will form the basis to develop a comprehensive image-method for modeling indoor wireless channels.

1.2 Background

The Sommerfeld half-space problem of electric dipole was defined by Arnold

Sommerfeld in 1909 in his paper "Propagation of waves in wireless telegraphy"^[16]. In this paper Sommerfeld tried to answer how the waves are propagated in wireless telegraphy, whether they are like Hertzian waves ("space waves") or electromagnetic waves ("surface waves"). According to Sommerfeld, wireless telegraphy waves consist of both Hertzian and electromagnetic waves, otherwise, Maxwell's equations and boundary conditions would not be satisfied. Sommerfeld's solution for vertical a dipole is defined by an integral which is not possible to evaluate in terms of elementary functions in a closed form. The integral around the pole of the integrand is a surface wave which is the same as Zenneck's surface wave at great distance. Sommerfeld had shown that electromagnetic waves can be transmitted along a wire of finite conductivity, and Zenneck stated that the Earth's surface acts as a conducting wire.

Throughout the years this paper has been of great interest for many scientists. Many agreed with Sommerfeld's solution from his 1909 edition of the problem. Nikola Tesla cited Sommerfeld's work as verification to his "World System" of wireless transmission in which Hertzian wave radiation is negligibly small compared to the entire energy manifested as "current waves" which were propagated through the ground by conduction^[17]. In 1930 Rolf developed curves describing variations of the field for all ground conditions^[18]. Unfortunately, all of the papers based on Sommerfeld's solution from 1909, including Rolf's, have a

sign error in them. Because of the sign error contained in Sommerfeld's 1909 paper it appears that Zenneck's wave does not exist.

Although Sommerfeld fixed the sign error in his 1926 paper, his solution started a heated debate soon after his 1909 paper. This debate continued on till the early 1950's. Many scientists argued in their papers that electromagnetic surface waves did not exist. The first question was raised by Weyl in 1919 who used a completely different method than Sommerfeld, and stated himself that his solution is not the same as Sommerfeld's. Banos^[19] later showed that although Sommerfeld and Weyl used different approaches, their formulation of the problem was equivalent. Even though Weyl had not made numerical checks, he should definitely be given credit for realizing the inconsistency with Sommerfeld's solution.

The first to notice a sign error in Sommerfeld's original solution was Norton in 1935. However, he never showed a detailed proof to his conclusions. Charles Burrows of Bell Labs looked closely at differences of Sommerfeld's and Weyl's formulation in 1936. In 1937 after a series of experiments he concluded that "The surface wave component of Sommerfeld is not set up by simple antennas on the surface of the Earth" such as modeled by Sommerfeld in his analysis^[20].

Even at this point, the debate was far from over. In 1947, Epstein published a paper in which he claims that the residue of the pole does not belong in the final

answer of the surface wave due to the fact that such a singularity does not exist^[21]. Bouwkamp^[22] proved him wrong in 1948, stating that he overlooked a singularity in his solution.

The debate on Sommerfeld's solution was put to stop by the work of Ott^[23], and Banos and Wesley^[24]. Ott properly clarified the existence of Sommerfeld's surface wave. In order to develop his saddle-point integration method for the existence of the first order pole, Ott had to combine Weyl's and Sommerfeld's methods, and therefore, re-derived Sommerfeld's formulation of the problem. Even Ott's great effort could not stop the debate completely. Banos and Wesley looked even closer into Sommerfeld's problem and pointed out discrepancy in papers that tried to prove Sommerfeld wrong. Banos summarized the work of the most significant contributors who helped clarified Sommerfeld's problem^[19].

Sommerfeld's paper from 1926 had a sign change and addition of one term that disappeared in the previous formulation due to the sign error. That term demonstrated characteristics of Zenneck's wave. Still, this did not change much since the existence of the wave is not determined upon one term, but the entire wave. Sommerfeld's 1926 solution proved the existence of surface waves for certain values of impedance and observation angles, and it proved that contribution to the complete field is dependent on distance.

Although the validity of Sommerfeld's solution is not questioned anymore, the interest in his paper did not disappear. Since limits of the Sommerfeld integral are infinite, many authors have dedicated time in developing various numerical and asymptotic techniques for its efficient evaluation. Many of the developed algorithms use various assumptions and approximations in order to give a closed form solution, and therefore, their solution is not exact.

One of the new techniques that was used to evaluate Sommerfeld's integral using an error-free approximations was the exact image theory. This method was originally proposed by Lindell and Alanen in 1984, for vertical electric and magnetic dipoles^[25] ^[26]. They noticed that singularities of the integrand also exist in a mirror image of the original dipole. This led them to express the reflection coefficient for the given image formulation, as a Laplace transform over an image source function. The final result is a rapidly convergent image integral. Based on Lindell's and Alanen's solution for electric dipole, Di and Gilbert^[27] extended the theory and applied it to local and extended reacting surfaces in acoustics.

Recent interests in Sommerfeld's problem focus more on its implementations and applications like using method of moments as an algorithm for perfectly conducting bodies of revolution for ground-penetrating radar^[28]. Time domain solution is used for evaluation of remote-sensing systems, for detection of shallow buried object, and probing the field in a geological medium. Both frequency and

time domain solutions are being researched and evaluated for indoor wireless applications^[29].

1.3 Problem Statement and Objectives

Despite the valuable contribution of the authors who worked on exact image theory method, they have lacked to outline the limitations and advantages of obtaining the entire field by this method. There is a need for significant improvement in the prediction.

As an emerging technology, the UWB signal brings many uncertainties and unknowns, especially in its interference with other wireless systems. Accurate prediction of propagation effect will allow to easier address other issues such as modulation, demodulation, coding schemes, power, and bandwidth which will help the optimization of appropriate design. It is the intent of this work to give an accurate and general model that can predict short-range/time UWB reflection. This reflection occurs when source and receiver are near a single reflecting boundary across which electric and magnetic fields are continuous. For instance, indoor wireless applications most likely have the transmitter and receiver mounted close to the wall or ceiling. In this kind of environment near-surface and near-field effects are likely to happen.

Our approach uses an image-based method based on a Laplace-transform formulation of the Sommerfeld's half-space problem. The boundary between two mediums is replaced by point source of given strength and location. Improvement to the originally proposed problem by Lindell and Alanen is a more simple solution of the total field. The complete field formulation is based on a simple branch-integral consisting of the reflection coefficient. Since the analysis is done in the frequency domain, the UWB pulse is recovered by an inverse Fourier transform.

In summary, the thesis will be comprised of five chapters. In Chapter 2 modulation and demodulation of UWB signals will be examined. The Laplace transform formulation of Sommerfeld half-space problem using exact image theory is given in Chapter 3. Chapter 4 shows the implementation of the solution gained in previous chapter. The UWB pulse is recovered by an inverse Fourier transform. Finally, Chapter 5 summarizes and concludes the thesis.

Chapter 2

BASIC PRINCIPLES OF MODULATION AND DEMODULATION

2.1 *Introduction*

In UWB systems pulse-trains are used to transmit symbols from source to receiver over the communication channel. The symbols to be transmitted are encoded using pulse position modulation (PPM). The data rate of the transmission is the ratio of the number bits encoded per pulse and time-average repetition period used between successive pulses. Because the transmitter is only operated over the pulse duration, UWB systems require lower power than that of conventional carrier based transmitters. However, additional processing is needed to modulate the pulse train and to shape its energy spectrum so that it does not interfere with conventional narrow band radio transmissions. To shape the spectrum, pseudo-random coding of the time-shifts may be used to minimize interference and jamming of narrow band receivers.

For a UWB system to be effective one need not to receive every pulse that is transmitted. Statistical inference of the transmitted symbol can be made from the statistical features derived from an ensemble comprised of many pulses. In order to recover the UWB signal in the presence of additive noise, a filter that yields

maximum output response to the input signal must be chosen. The most often used filter for this purpose is the matched filter.

In this chapter we will discuss the basic principles of modulating the binary data using PPM, and demodulating the received signal with the matched filter.

2.2 *Pulse Position Modulation*

In this section we will present how a binary data sequence is modulated using the PPM method. In PPM, data to be transmitted is encoded into the time delay between transmitted pulses. The time delay for the l^{th} symbol will be defined as τ_l where its magnitude is related to the symbol being transmitted. Given a sequence of input symbols the transmission takes the form of a pulse train $s(t)$.

$$s(t) = \sum_{l=0}^{\infty} p(t - \tau_l) \quad (2.1)$$

where the function $p(t)$ is the monocycle Gaussian waveform

$$p(t) = \frac{t}{\sigma^2} e^{-\frac{t^2}{2\sigma^2}} \quad (2.2)$$

This pulse is generated by applying Gaussian time varying voltage $v(t)$ to a dipole antenna.

$$v(t) = -V_0 e^{-\frac{t^2}{2\sigma^2}} \quad (2.3)$$

The temporal pulse width of the input voltage is equal to σ . The spectrum of the input voltage $V(\omega)$ can be obtained applying the Fourier transform to $v(t)$.

$$V(\omega) = -V_0 \sigma \sqrt{2\pi} e^{-\frac{\omega^2 \sigma^2}{2}} \quad (2.4)$$

For the dipole antenna, the generated electric field strength is proportional to the time derivative of the source supplied current, $i(t)$. As a result $p(t)$ will be proportional to $\frac{di}{dt}$. If one considers the impedance of the antenna, R , to be real valued, the time derivative of the current is

$$i'(t) = \frac{1}{R} \frac{dv}{dt} \quad (2.5)$$

The spectrum of the time derivative of the current is equal to $\frac{j\omega}{R} V(\omega)$ with current's amplitude defined as $I_0 = V_0/R$. Therefore, the time derivative of the

current will be Gaussian monocycle with a non-zero center frequency. The Fourier transform of $i'(t)$ is

$$I'(\omega) = I_0 j \omega \sigma \sqrt{2\pi} e^{-\frac{\omega^2 \sigma^2}{2}} \quad (2.6)$$

The center frequency of $I'(\omega)$ is evaluated at the centroid of $I'(\omega)$ with respect to ω .

$$\omega_c = \frac{\int_0^{\infty} \omega I'(\omega) d\omega}{\int_0^{\infty} I'(\omega) d\omega} = \frac{\sqrt{\pi}}{\sigma\sqrt{2}} \approx \frac{1.25}{\sigma} \quad (2.7)$$

The second moment of $I'(\omega)$ with respect to $(\omega - \omega_c)^2$ yields the square of the bandwidth of the Fourier transform of the pulse.

$$\omega_{bw} = \sqrt{\frac{\int_0^{\infty} (\omega - \omega_c)^2 I'(\omega) d\omega}{\int_0^{\infty} I'(\omega) d\omega}} = \frac{\sqrt{4 - \pi}}{\sqrt{2}\sigma} \approx \frac{0.66}{\sigma} \quad (2.8)$$

Hence, for a short time duration pulse, $\sigma \ll 1$, the center frequency and bandwidth is $O(1/\sigma)$.

Initially, $p(t)$ starts at zero-time on the transmitter's clock, but it gets shifted by the amount of τ_l , where τ_l is defined as

$$\tau_l = lT_f + m\Delta t + \tilde{T}_l \quad (2.9)$$

As we can see the time-shift is comprised of three terms. The variable T_f represents the frame period. During each frame period only one pulse is transmitted. A uniform pulse signal would be defined as $\sum_{l=0}^{\infty} p(t - lT_f)$, where T_f is a fixed duration of each time frame or pulse repetition time. The variable Δt represents the incremental time shift to be used to encode a given symbol. We will consider Δt to be equal to the width of the Gaussian monocycle pulse. The symbol given by the index m will be shifted by $m\Delta t$. For a binary data one may label the data 0 and 1 as $m = 0$ and $m = 1$ respectively.

With $\tilde{T}_l = 0$, and with the occurrence of m equal to 0 or 1 being equally probable and statistically independent, the pulse train, $x(t)$, is defined as

$$x(t) = \sum_{l=0}^{\infty} \delta(t - lT_f - m\Delta t) \quad (2.10)$$

where $\delta(t)$ is Dirac function. As mentioned previously, transmission takes place using the Gaussian monocycle given in Eqn(2.2), with the given encoded time delay. Without \tilde{T}_l , $s(t)$ takes the following form,

$$s(t) = \sum_{l=0}^{\infty} p(t - lT_f - m\Delta t) \quad (2.11)$$

One can consider $s(t)$ as being the result of convolution $x(t)*p(t)$, where

$x(t) = \sum_{l=0}^{\infty} \delta(t - lT_f - m\Delta t)$. In order to find the power spectral density of $s(t)$, we

need to find the power spectral density of $x(t)$ and $p(t)$. Power spectral density of $s(t)$ is defined as

$$S_{ss}(\omega) = S_{xx}(\omega)S_{pp}(\omega) \quad (2.12)$$

where $S_{xx}(\omega)$ and $S_{pp}(\omega)$ are power spectral densities of $x(t)$ and $p(t)$ respectively.

Power spectral density of $p(t)$ is simply the squared magnitude of the Fourier transform of $p(t)$

$$S_{pp}(\omega) = |P(\omega)|^2 \quad (2.13)$$

Since the pulse is generated as a time varying voltage, $v(t)$, and the transmitted field is proportional to the $i'(t)$, we can represent the power spectral density of $p(t)$ as

$$S_{pp}(\omega) = |I'(\omega)|^2 \quad (2.14)$$

where $I'(\omega)$ is given in Eqn (2.6). Power spectral density of $x(t)$ is the Fourier transform of its auto-correlation function, $R_{xx}(\tau)$, where $R_{xx}(\tau)$ is obtained through the expression

$$R_{xx}(\tau) = \frac{1}{N} \int_0^{NT_f} x(t)x(t+\tau)dt \quad (2.15)$$

where N is the frame number. Figure 2.1 shows $R_{xx}(\tau)$ completed by simulation for $T_f \geq 0$, and $R_{xx}(\tau)$ is symmetric on the both sides of $T_f = 0$. By observation, $R_{xx}(t)$ yields the following expression

$$\begin{aligned}
R_{xx}(t) = & \frac{1}{2} \sum_{l=-\infty}^{\infty} \delta(t - lT_f) + \frac{1}{4} \sum_{l=-\infty}^{\infty} \delta(t - lT_f + \Delta t) + \frac{1}{4} \sum_{l=-\infty}^{\infty} \delta(t - lT_f - \Delta t) \\
& + \frac{1}{2} \delta(t) - \frac{1}{4} \delta(t - \Delta t) - \frac{1}{4} \delta(t + \Delta t)
\end{aligned} \quad (2.16)$$

Fourier series coefficients of $R_{xx}(t)$ are

$$S_{xx} = \frac{1}{T_f} \left[\frac{1}{2} + \frac{1}{4} e^{-j\omega_0 k \Delta t} + \frac{1}{4} e^{j\omega_0 k \Delta t} \right] + \frac{1}{2} - \frac{1}{4} e^{-j\omega \Delta t} - \frac{1}{4} e^{j\omega \Delta t} \quad (2.17)$$

where fundamental frequency $\omega_0 = \frac{2\pi}{T_f}$. Therefore, the power spectral density of

$x(t)$ can be written as

$$S_{xx}(\omega) = \frac{\pi}{T_f} \left[\sum_{l=-\infty}^{\infty} \left[1 + \cos(\omega_0 l \Delta t) \right] \delta(\omega - l\omega_0) \right] + \pi [1 - \cos(\omega \Delta t)] \quad (2.18)$$

If we consider formulations of power spectral densities of $x(t)$ and $p(t)$, we can re-express the power spectral density of $s(t)$ as

$$S_{ss}(\omega) = \left(\frac{\pi}{T_f} \left[\sum_{l=-\infty}^{\infty} \left[1 + \cos(\omega_0 l \Delta t) \right] \delta(\omega - l\omega_0) \right] + \pi [1 - \cos(\omega \Delta t)] \right) |I'(\omega)|^2 \quad (2.19)$$

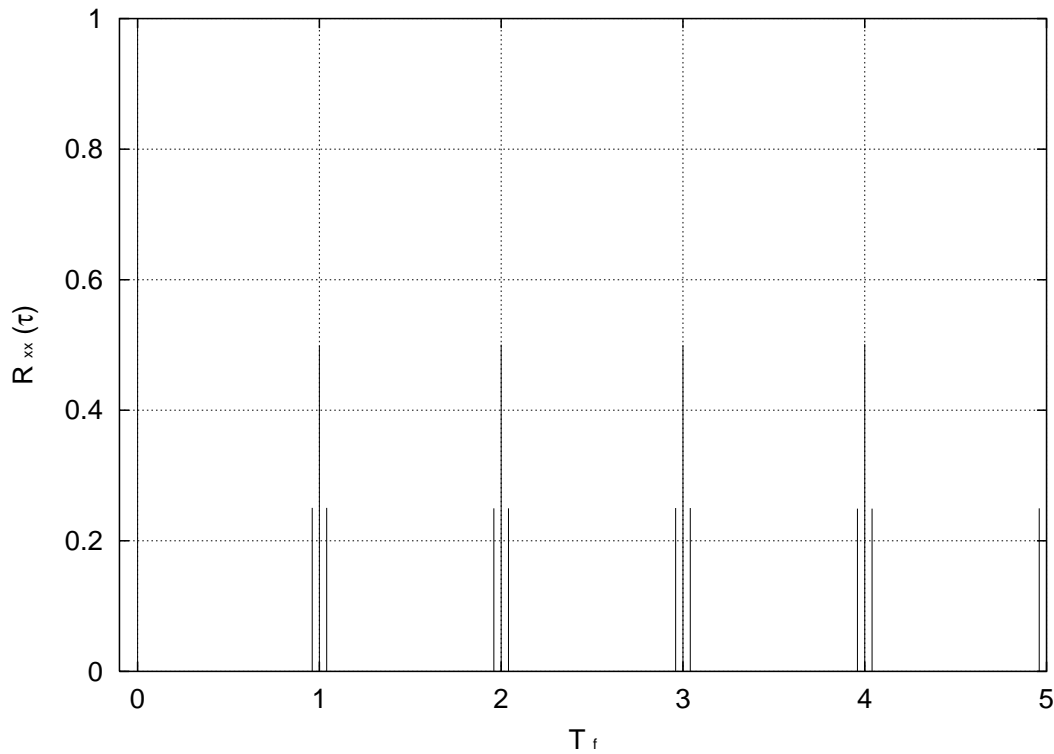


Figure 2.1. Auto-correlation of $x(t)$

As we can see in the aforementioned expression, $S_{ss}(\omega)$ is the sum of the discrete and continuous spectrum. Spectral nulls in the continuous spectrum occur at even integral multiples of $\pi/\Delta t$, and spectral nulls of discrete spectrum occur at $\frac{(2n+1)\pi}{\Delta t}$ for integral values of n . This feature can be used to advantage when one needs to guard a particular frequency for interference from the UWB signal. Sampling of the spectrum is the result of the periodicity introduced by the periodic

frame interval. Sampling can be problematic if the frequency $l\omega_0$ corresponds to a guarded frequency. This means that by the careful design of the pulse shape, being able to manipulate the value of Δt , we can minimize UWB interference by creating spectral nulls in regions where interference is problematic.

In order to flatten the spectrum, the l^{th} monocycle of $p(t)$ can be shifted by additional amount, \tilde{T}_l , where \tilde{T}_l is generated as a random number. A requirement to demodulate the signal is that the receiver random numbers be synchronized with the transmitters random number sequence. In Figure 2.2 two superimposed bits, "1" and "0", are shown in a single frame interval of 0.2 ns , where we chose $\sigma = 10^{-9} \text{ s}$. Both pulses are originally positioned at $t = 0$. It can be seen that for this example the pulse representing bit "0" is not shifted as much as the pulse representing bit "1".

The shift of Δt does not apply to "0" bit, since $m = 0$. Although, this is not the universal case, both of the pulses are shifted by some random number, \tilde{T}_l , and they might appear in any of the compartments within the frame. In this case, \tilde{T}_l was generated with uniform pseudo-random number generator.

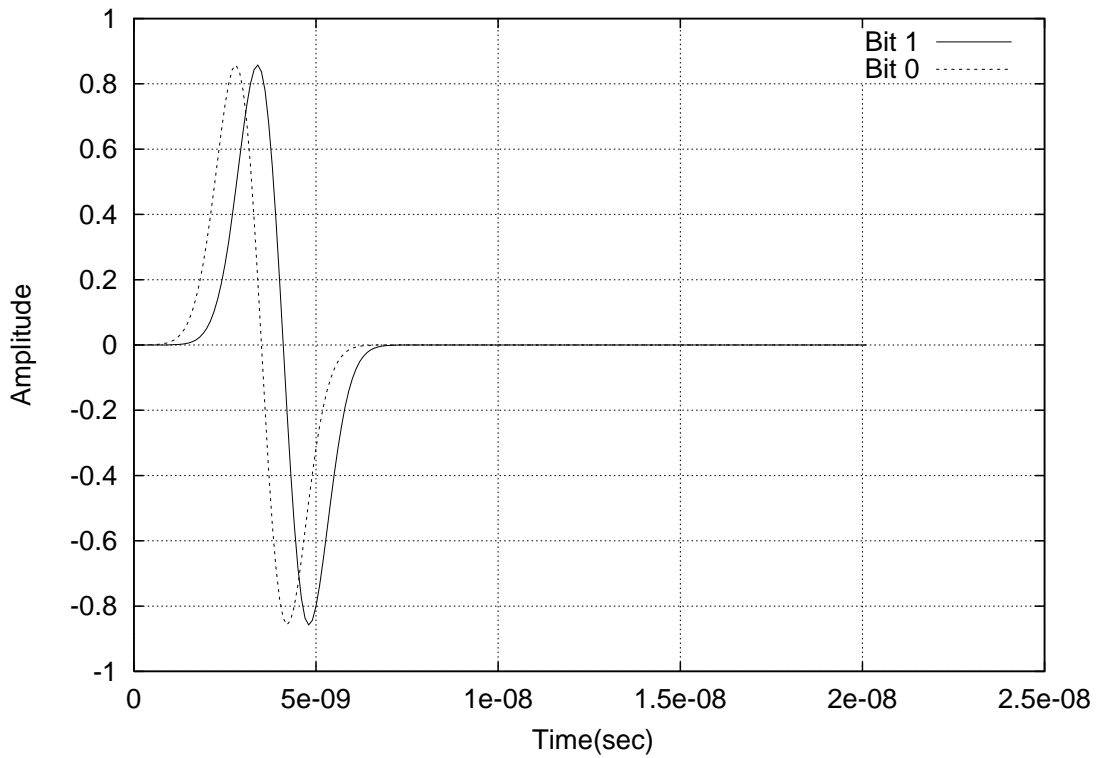


Figure 2.2. Superimposed plot of two bits in a single frame

A sample of the modulated signal by PPM is shown in Figure 2.3. In Figure 2.3 five consecutive frames are shown. Sampling time for this given example is

$$T_s = \frac{2\pi}{\omega_c + \omega_{bw}},$$

where ω_c and ω_{bw} are previously defined in Eqns (2.7) and (2.8)

respectively. Each frame time is defined as $T_f = 10T_s$. Because of time-hopping codes monocytes are not uniformly spread within frames, which makes the pulse-overlaps less likely to happen.

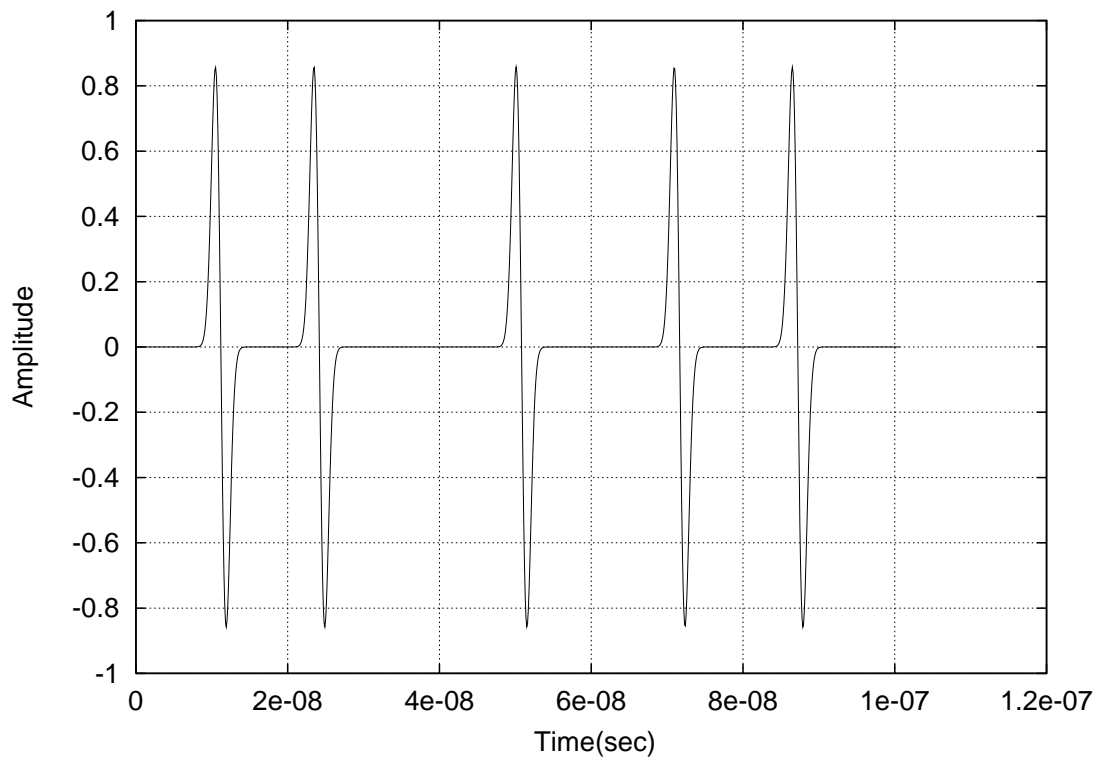


Figure 2.3. Sample of modulated signal $\{1, 0, 1, 1, 0\}$

2.3 Matched Filter Demodulation

In this section we will examine the process of detection of a pulse in the presence of additive white noise, $n(t)$. The signal is modified as

$$s(t) = \sum_{l=-\infty}^{\infty} p(t - \tau_l) + n(t) \quad (2.20)$$

In order to demodulate the signal, one must mediate the influence of $n(t)$ at the receiver. One way to do so is to use a matched filter. A general block diagram of the matched filter is shown in Figure 2.4, where $s(t)$ is the PPM signal, $n(t)$ is the noise signal, and $h_M(t)$ is the filter impulse response. The resulting signal is $s_0(t) + n_0(t)$.

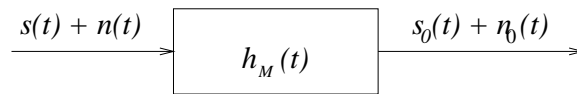


Figure 2.4. Block diagram of the matched filter

The matched filter yields the maximum output response to the input signal in the presence of additive noise^[30]. The objective is to maximize the signal to noise ratio at $t = t_m$. Using the energy, the ratio that needs to be maximized is

$$\frac{|s_0(t_m)|^2}{\overline{n_0^2(t)}} \quad (2.21)$$

where $\overline{n_0^2(t)}$ is the mean-square noise output of the matched filter. The filtered signal $s_0(t)$ can be defined through the inverse Fourier transform as

$$s_0(t) = \frac{1}{2\pi} \int_{-\infty}^{\infty} H_M(\omega) S(\omega) e^{j\omega t} d\omega \quad (2.22)$$

where $S(\omega)$ and $H_M(\omega)$ are Fourier transforms of $s(t)$ and $h_M(t)$ respectively.

Similarly, $s_0(t)$ at $t = t_m$ can be expressed as

$$s_0(t_m) = \frac{1}{2\pi} \int_{-\infty}^{\infty} H_M(\omega) S(\omega) e^{j\omega t_m} d\omega \quad (2.23)$$

The power spectral density of the noise is $S_{nn}(\omega) = \frac{\eta}{2}$ where η is the variance of the noise for half of the spectrum. Therefore, the mean-square of the noise amplitude is

$$\overline{n_0^2(t)} = \frac{1}{2\pi} \int_{-\infty}^{\infty} \frac{\eta}{2} |H_M(\omega)|^2 d\omega \quad (2.24)$$

With substitution of Eqns (2.23) and (2.24) into Eqn (2.21) the expression of squared signal to noise ratio results in

$$\frac{|s_0(t_m)|^2}{n_0^2(t)} = \frac{\left| \int_{-\infty}^{\infty} H_M(\omega) S(\omega) e^{j\omega t_m} d\omega \right|^2}{\pi \eta \int_{-\infty}^{\infty} |H_M(\omega)|^2 d\omega} \quad (2.25)$$

In order to simplify the numerator's expression in the signal to noise ratio, the Schwartz inequality is introduced

$$\left| \int_{-\infty}^{\infty} f_1(x) f_2(x) dx \right|^2 \leq \int_{-\infty}^{\infty} |f_1(x)|^2 dx \int_{-\infty}^{\infty} |f_2(x)|^2 dx \quad (2.26)$$

The equality in Eqn (2.26) occurs when $f_1(x) = k_c f_2^*(x)$. Assuming that $f_1(x)$ is FFT of filter's transfer function, $H_M(\omega)$, and $f_2(x)$ is FFT of PPM signal, $S(\omega)$, Schwartz inequality is expressed as

$$\left| \int_{-\infty}^{\infty} H_M(\omega) S(\omega) e^{j\omega t_m} d\omega \right|^2 \leq \int_{-\infty}^{\infty} |H_M(\omega)|^2 d\omega \int_{-\infty}^{\infty} |S(\omega)|^2 d\omega \quad (2.27)$$

For the constraint where signal-to-noise ratio needs to be maximum, substitution of Eqn (2.27) into Eqn (2.25) yields

$$\frac{|s_0(t_m)|^2}{n_0^2(t)} = \frac{1}{\pi\eta} \int_{-\infty}^{\infty} |S(\omega)|^2 d\omega \quad (2.28)$$

For condition of equality to be satisfied,

$$H_M(\omega) = k_c S^*(\omega) e^{-j\omega t_m} \quad (2.29)$$

or in time domain,

$$h_M(t) = k_c s^*(t_m - t) \quad (2.30)$$

Arbitrary constant k_c is assumed to be 1 for convenience in further analysis. This draws the conclusion that the impulse response of the filter, $h_M(t)$, is equal to the complex conjugate of the signal, $s(t)$ delayed by the sampling time, t_m . With the given information, the block diagram of the matched filter is shown in Figure 2.5.

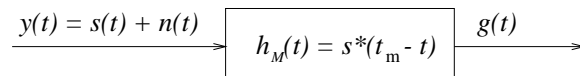


Figure 2.5. Block diagram of the matched filter

The signal $y(t)$ represents the modulated UWB signal with additive noise, which is put through the matched filter giving the output signal $g(t)$. This definition of matched filter requires that the signal $s(t)$ is known apriori. The output signal $g(t)$ represents the convolution of the input signal $y(t)$ with the impulse response of the filter $s^*(t_m - t)$

$$g(t) = s^*(t_m - t) * y(t) = \int_{-\infty}^{\infty} s^*(t_m - \xi) y(t - \xi) d\xi \quad (2.31)$$

The expression for the filtered signal can be further simplified, with the substitution $\gamma = t_m - \xi$. Now, the expression for $g(t)$ is

$$g(t) = \int_{-\infty}^{\infty} s^*(\gamma) y(\gamma + t - t_m) d\gamma \quad (2.32)$$

This expression defines $g(t)$ as time cross-correlation function between $s(t)$ and $y(t)$

$$g(t) = R_{sy}(t - t_m) \quad (2.33)$$

Keeping in mind that $y(t) = s(t) + n(t)$, $g(t)$ becomes the sum of auto-correlation of

the signal and cross-correlation between signal, $s(t)$, and noise, $n(t)$

$$g(t) = R_{ss}(t - t_m) + R_{sn}(t - t_m) \quad (2.34)$$

If cross-correlation of $s(t)$ and $n(t)$ is zero then the peak output is given by $R_{ss}(0)$

that is at $t = t_m$, where

$$R_{ss}(\tau) = \int_{-\infty}^{\infty} s^*(\gamma)s(\gamma + \tau)d\gamma \quad (2.35)$$

and $\tau = t - t_m$. The block diagram of the cross-correlator is given in Figure 2.6. The output of the multiplier is integrated in order to get $R_{sy}(t_m)$.

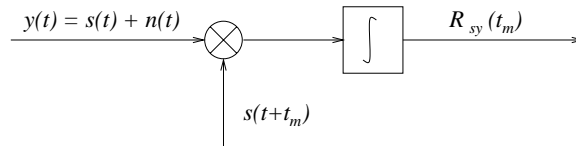


Figure 2.6. Block diagram of the matched filter correlator

Figure 2.7 shows two pulses; one is a pulse without additive noise, $s(t)$, and other is the same pulse with additive noise, $y(t)$. In this case we have assumed ideal

propagation conditions and Gaussian distributed additive noise with the mean of 0.024147 and variance of 1.03433.

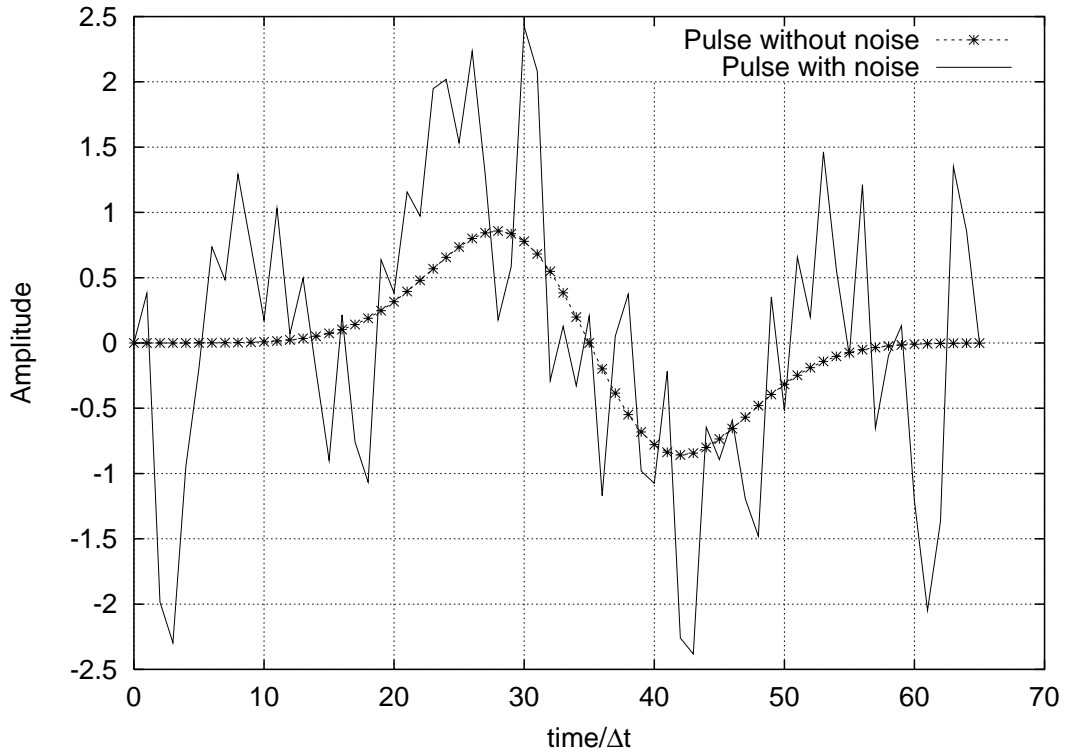


Figure 2.7. Comparison of pulse with the noise and pulse without the noise

Pulses from Figure 2.7 are passed through the matched filter. The result of the correlation shown in Figure 2.8 compares the ideal noiseless signal and the actual filtered received signal with additive noise applied. Signal to noise ratio for the

pulse in Figure 2.8 is -6.56 dB.

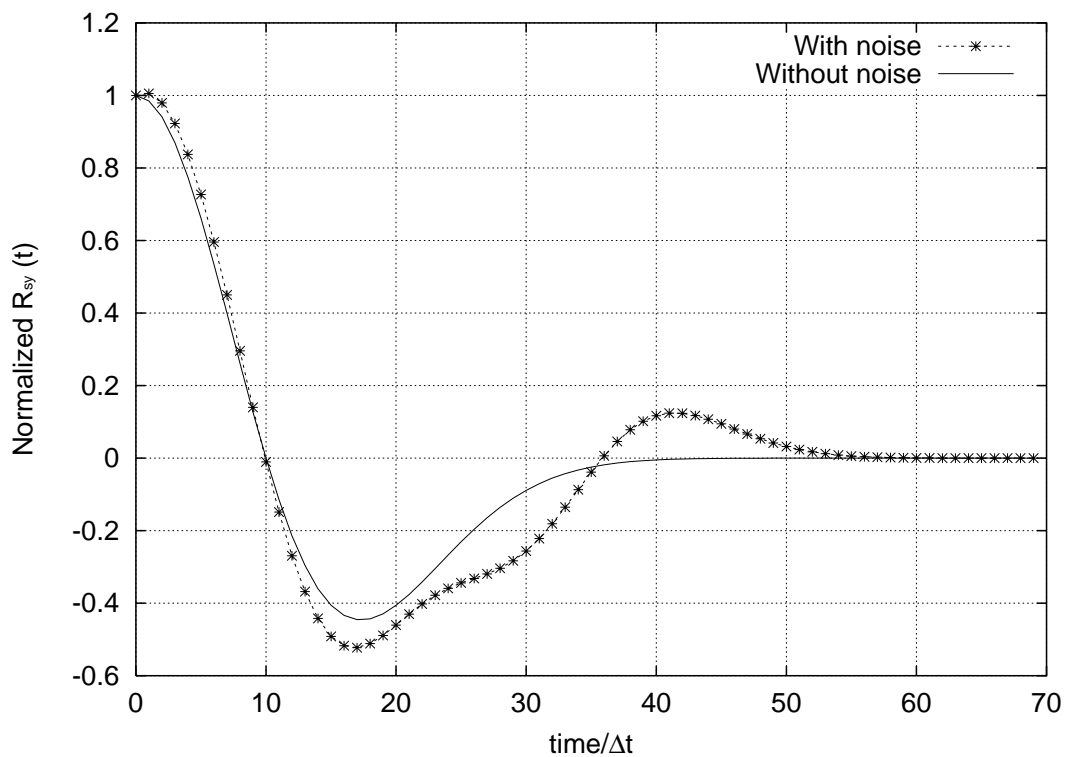


Figure 2.8. Response of the matched filter for one realization

Information of UWB signal does not strictly depend on one pulse. For one information symbol, approximately 1000 pulses are sent from transmitter to receiver. Figure 2.9 represents response of the matched filter for 1000 realizations.

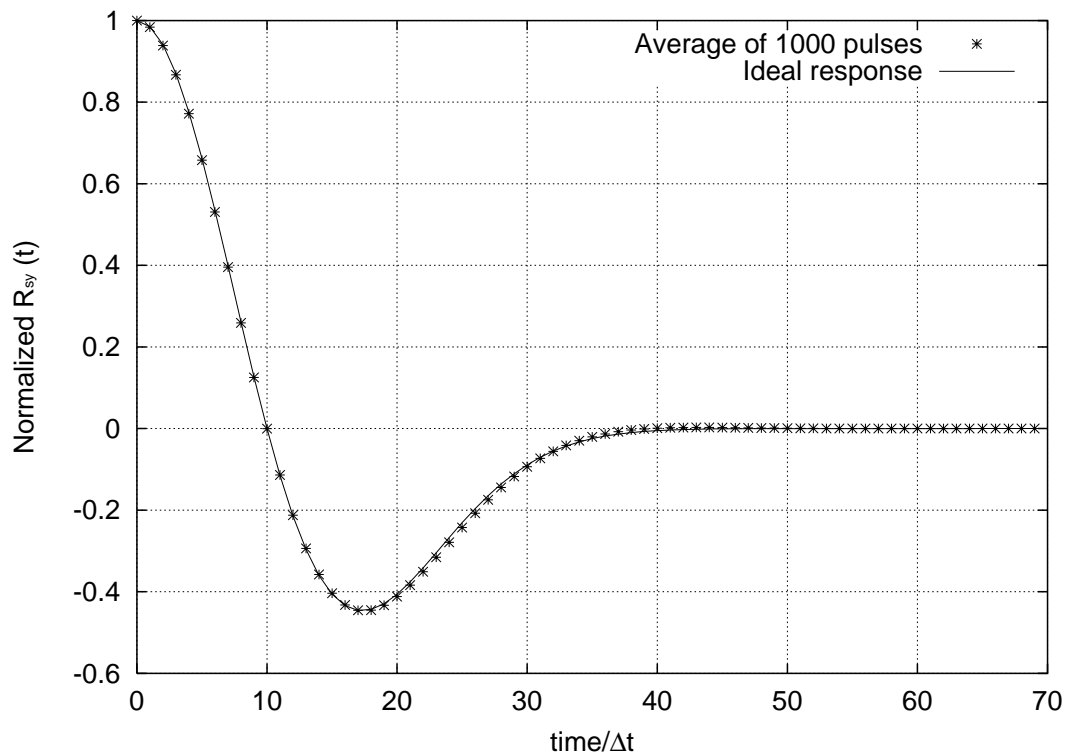


Figure 2.9. Response of the matched filter averaging 1000 realizations

When the receiver is synchronized with the transmitter, it can detect the delay between the expected and actual pulse arrival time, and it must determine whether or not a pulse from the transmitter was delayed relative to its anticipated position. Since transmitter is using randomly generated numbers for PPM, the receiver needs to use the same random number generator in order to be synchronized with receiver and to be capable of affective demodulation.

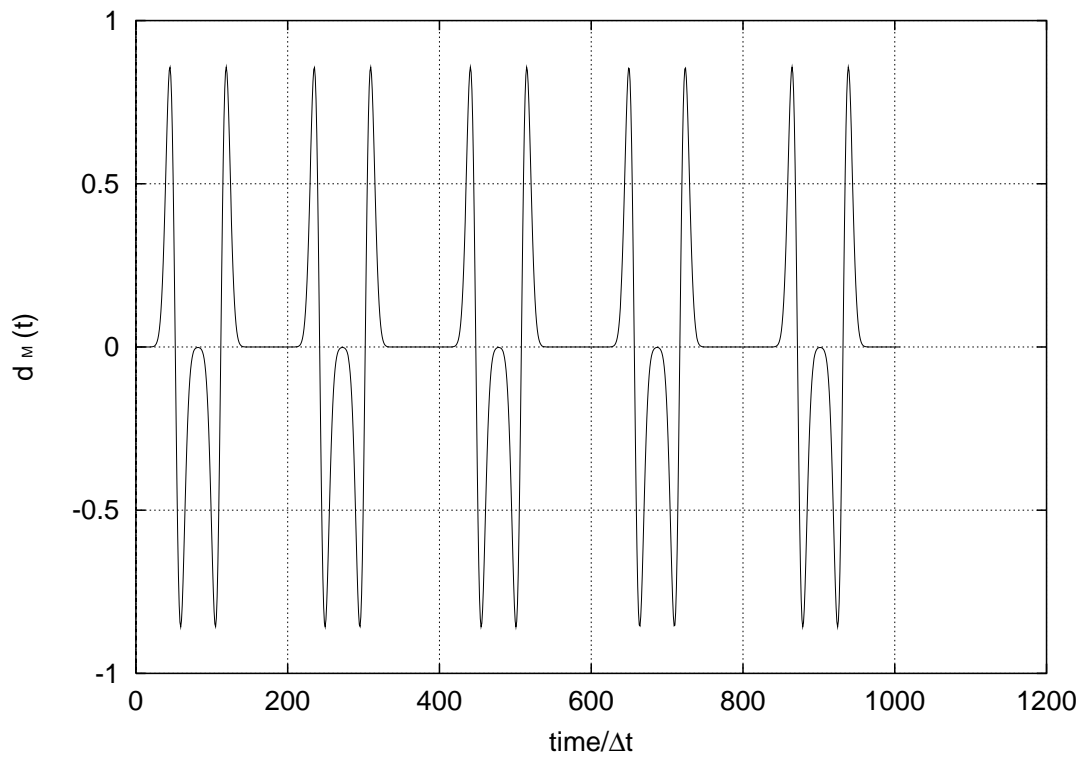


Figure 2.10. Correlator described in Eqn (2.36)

The receiver is a bit duration correlator employing

$$d_M(t) = p(t - \tilde{T}_l) - p(t - \Delta t - \tilde{T}_l) \quad (2.36)$$

The received signal $s(t)$, is demodulated with the correlator signal $d_M(t)$. The correlator is comprised of two terms. Both of the terms represent Gaussian monocycles with the same characteristics as the pulse used in the modulation.

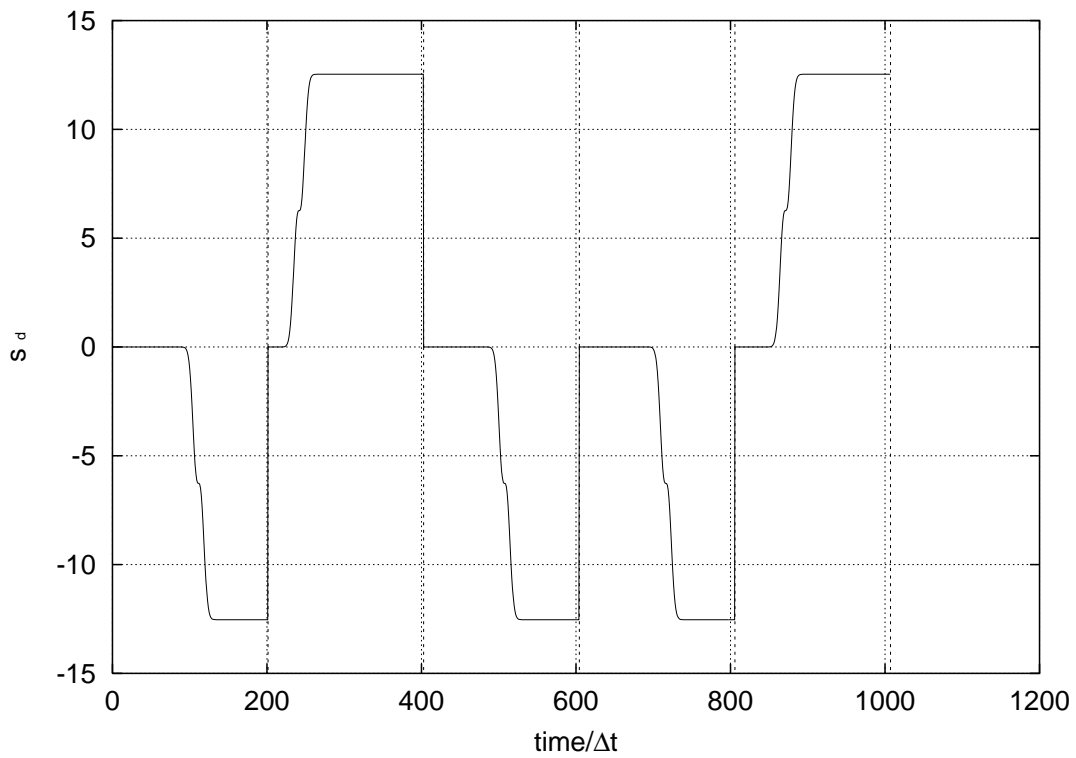


Figure 2.11. Demodulated signal $\{1,0,1,1,0\}$

However, the first term of the correlator $p(t - \tilde{T}_l)$ is the pulse shifted only by a random number, \tilde{T}_l , as bit "0" was shifted during the modulation. Similarly, second term of the correlator $p(t - \Delta t - \tilde{T}_l)$ is the pulse shifted by the same amount bit "1" was shifted in the modulation. The correlator, $d_M(t)$, is shown in Figure 2.10.

In order to determine whether "0" or "1" has been transmitted, the demodulated signal, $s_d(t)$, is compared with zero-threshold, where

$$s_d(t) = \int_{t=0}^{T_f} s(t)d_M(t)dt \quad (2.37)$$

If the value of the integral over the frame is larger than 0 then transmitted bit is set to "0", and if the value of the integral over the frame is less than 0 then transmitted bit is set to "1". Figure 2.11 represents the demodulated signal shown in Figure 2.3.

Chapter 3

SPHERICAL WAVE REFLECTION FROM A PLANAR INTERFACE

3.1 Introduction

To faithfully transmit data from the source to the receiver one must consider and in many cases mediate impairments introduced by the intervening media. In indoor wireless communications these impairments are the result of reflections from walls and obstacles in a room or building. These reflections or multipath signals modify the frequency response of the channel and interfere with the line of sight signal being detected at the receiver. The short time duration and relatively long repetition time of ultra wideband pulses make them less susceptible to multipath interference. However, multipath does affect the SNR and may become a problem if the repetition time is decreased.

In this chapter we will evaluate the reflection of a spherical wave generated by a dipole antenna from a planar surface. The amplitude and spatial characteristics of the reflected wave will also be examined. To do so, an exact image theory based on the Laplace transform is introduced. It is shown that a branch integral can be used to solve for the image source contribution. The integrand is convergent, and accuracy by numerical evaluation is easily established.

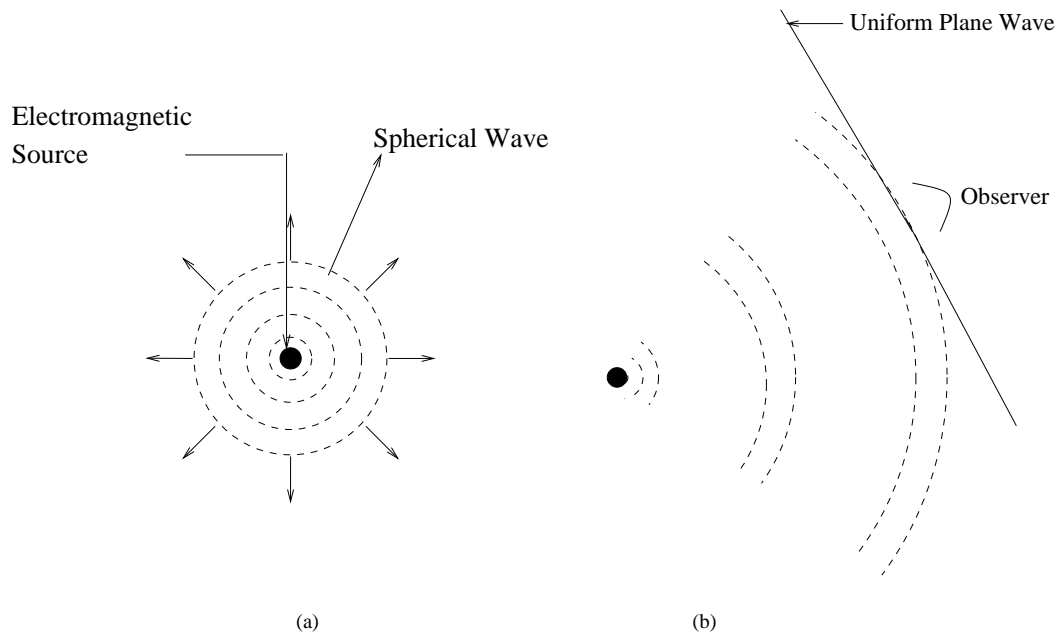


Figure 3.1. Energy generation by electromagnetic source (a) Spherical Wave (b) Plane-wave approximation at oblique incidence

In long range propagation problems, where the source to receiver distance is much greater than a wavelength, the assumption is that reflection coefficient of the spherical wave is essentially identical to that derived using plane wave theory. When a point electromagnetic source emits energy, the energy spreads outwardly from the source along the wavefront. To an observer in the far-field, the wave

appears planar as it was a part of a uniform planar wave (Figure 3.1). In indoor propagation the plane wave approximation will be of limited utility when near-field estimates of the amplitude are required.

The polarized wave units of the reflection and transmission coefficients can be decomposed, using superposition, into its parallel and perpendicular polarized components. In radio waves, it is common to designate wave polarization by the plane of the electric field vector. If the electric field vector lies parallel to the plane of incidence than the radio waves are characterized as parallel-polarized. If electric field vector lies perpendicular to the plane of incidence the radio waves are classified as perpendicular-polarized. Therefore, the incident wave (\vec{E}_i, \vec{H}_i) is decomposed into perpendicular-polarized component $(\vec{E}_{i\perp}, \vec{H}_{i\perp})$ and parallel-polarized component $(\vec{E}_{i\parallel}, \vec{H}_{i\parallel})$.

3.2 *Free Space Propagation*

In the previous chapter it was mentioned that the pulses are transmitted as Gaussian monocycles. Therefore, only the case where the voltage is produced as a Gaussian monocycle shall be considered. Since voltage is Gaussian shaped in time (Eqn (2.3)), the current has Gaussian form as well. It is represented as,

$$i(t) = \frac{V_0}{R} e^{-\frac{t^2}{2\sigma^2}} = i_0 e^{-\frac{t^2}{2\sigma^2}} \quad (3.1)$$

where R is the resistance, and i_0 is the current's peak value. For further analysis the current will be referred to by its peak value, and multiplication by the factor $e^{-\frac{t^2}{2\sigma^2}}$ is to be understood. The Fourier transform of $i(t)$ will be expressed as $I_0(\omega)$. When the current is known, the customary approach for finding the electric and magnetic fields at the observer point, $O(r, \theta, \phi)$, is by using the retarded magnetic vector potential \bar{A} . The geometry is depicted in Figure 3.2. The current is assumed to have only z component.

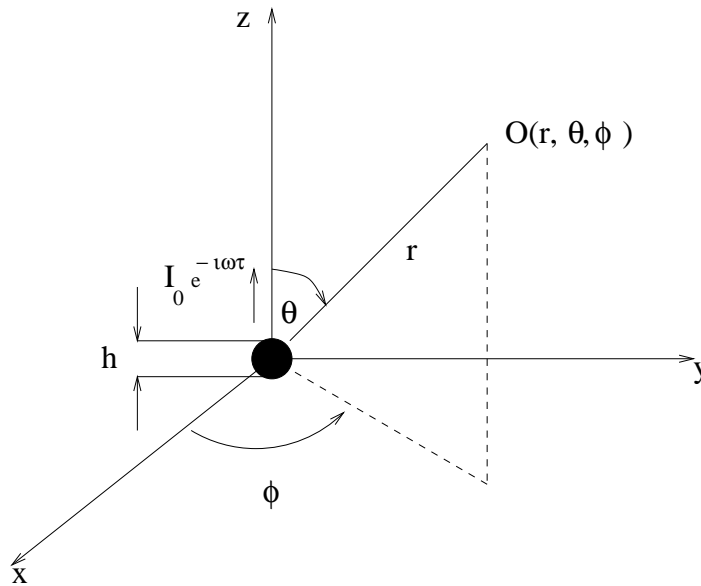


Figure 3.2. Electric dipole and the spherical coordinate system

Therefore, the retarded vector potential has only the z component. The Fourier amplitude of the retarded vector potential is defined as

$$A_z = \mu_0 \frac{hI_0}{4\pi r} e^{jkr} \quad (3.2)$$

where r is the distance between the source and the observer, h is the diameter of the source, I_0 is the Fourier transform of i_0 , and the wavenumber $k = \frac{\omega}{c}$. The spherical components of \bar{A} are found as follows

$$A_r = A_z \cos \theta = \mu_0 \frac{hI_0}{4\pi r} e^{jkr} \cos \theta \quad (3.3)$$

$$A_\theta = -A_z \sin \theta = -\mu_0 \frac{hI_0}{4\pi r} e^{jkr} \sin \theta \quad (3.4)$$

The orientation of the source renders the ϕ component of \bar{A} equal to zero. The vector components of the electric and magnetic fields can be found from the spherical components of \bar{A}

$$\bar{H} = \frac{1}{\mu_0} \nabla \times \bar{A} \quad (3.5)$$

$$\bar{E} = \frac{1}{-j\omega\epsilon_0} \nabla \times \bar{H} \quad (3.6)$$

The spherical components of magnetic and electric fields are

$$H_\phi = \frac{I_0 h}{4\pi} e^{jkr} \left(\frac{-jk}{r} + \frac{1}{r^2} \right) \sin \theta \quad (3.7)$$

$$E_r = \frac{I_0 h}{4\pi} e^{jkr} \left(\frac{2\eta_0}{r^2} + \frac{2}{-j\omega\epsilon_0 r^3} \right) \cos \theta \quad (3.8)$$

$$E_\theta = \frac{I_0 h}{4\pi} e^{jkr} \left(\frac{-j\omega\mu}{r} + \frac{\eta_0}{r^2} + \frac{1}{-j\omega\epsilon_0 r^3} \right) \sin \theta \quad (3.9)$$

where $\eta_0 = \sqrt{\mu_0/\epsilon_0}$. The terms containing $\frac{1}{r}$ are considered to be far-field components, whereas the $\frac{1}{r^2}$ and $\frac{1}{r^3}$ terms are considered near-field components.

At large distances from the source the only terms $O\left(\frac{1}{r}\right)$ are retained. Therefore,

expressions for electric and magnetic fields can be simplified to

$$H_\phi \cong \frac{-jkI_0 h}{4\pi r} \sin \theta e^{jkr} \quad (3.10)$$

$$E_{\theta} \cong \frac{-j\omega\mu_0 I_0 h}{4\pi r} \sin\theta e^{jkr} \quad (3.11)$$

Inverting the Fourier transforms given by Eqns (3.10) and (3.11), and using $k \frac{\omega}{c}$, yields

$$h_{\phi}(t) \cong \frac{h}{4\pi rc} \frac{d}{dt} i_0 \left(t - \frac{r}{c} \right) \sin\theta \quad (3.12)$$

$$e_{\theta}(t) \cong \frac{\mu_0 h}{4\pi r} \frac{d}{dt} i_0 \left(t - \frac{r}{c} \right) \sin\theta \quad (3.13)$$

Thus, the field strength of the electric dipole varies as the first time-derivative of the current. For different antennas the relationship between the current and field strength might be different, however, the field never varies like the antenna current. Radiation of the antenna is caused by the acceleration of charges which is proportional to the first derivative of the current, not by their constant motion^[31].

3.3 Parallel Polarization

The geometry used to describe the reflection of a parallel-polarized wave from a planar interface is shown in Figure 3.3. The planar boundary at $z = 0$

separates two mediums. Medium 1 occupies $z < 0$, and medium 2 occupies remainder of the space. Incident electric field vector, $\vec{E}_{i\parallel}$, is parallel to the plane of incidence, and incidence magnetic field vector, $\vec{H}_{i\parallel}$, is perpendicular to the plane of incidence. Therefore, the condition that $\vec{E}_{i\parallel} \times \vec{H}_{i\parallel}$ should result in incident propagating wave is derived along \vec{k}_i .

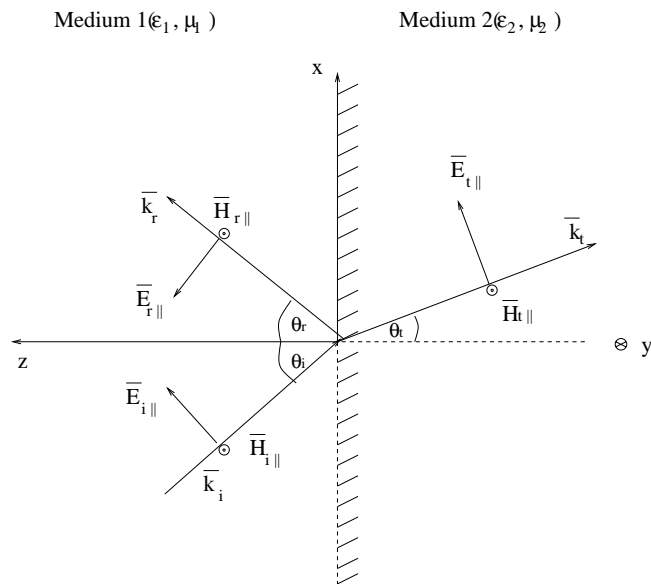


Figure 3.3. Parallel-polarized plane wave incident at an angle θ_i upon planar boundary

Assuming a $e^{-j\omega t}$ time dependence the propagating incident wavenumber vector \vec{k}_i is given by

$$\bar{k}_i = k_1[\hat{x} \sin \theta_i - \hat{z} \cos \theta_i] \quad (3.14)$$

where k_1 is wavenumber of medium 1 characterized by its electric permittivity, ϵ_1 , and magnetic permeability, μ_1 . Wavenumber, k_1 , is defined as $k_1 = \omega\sqrt{\mu_1\epsilon_1}$.

Similarly, reflected and transmitted waves can be expressed as

$$\bar{k}_r = k_1[\hat{x} \sin \theta_r + \hat{z} \cos \theta_r] \quad (3.15)$$

$$\bar{k}_t = k_2[\hat{x} \sin \theta_t - \hat{z} \cos \theta_t] \quad (3.16)$$

where θ_r and θ_t are reflection and transmission angles shown in Figure 3.3. The position vector is $\bar{r} = [z\hat{z} + x\hat{x}]$. The electric fields for plane waves can be expressed as

$$\bar{E}_{i\parallel}(z) = E_{0\parallel}^i(\hat{x} \cos \theta_i + \hat{z} \sin \theta_i)e^{j\bar{k}_i \cdot \bar{r} - j\omega t} \quad (3.17)$$

$$\bar{E}_{r\parallel}(z) = -E_{0\parallel}^r(\hat{x} \cos \theta_r - \hat{z} \sin \theta_r)e^{j\bar{k}_r \cdot \bar{r} - j\omega t} \quad (3.18)$$

$$\bar{E}_{t\parallel}(z) = E_{0\parallel}^t(\hat{x} \cos \theta_t + \hat{z} \sin \theta_t)e^{j\bar{k}_t \cdot \bar{r} - j\omega t} \quad (3.19)$$

where the quantities $E_{0\parallel}^i$, $E_{0\parallel}^r$, and $E_{0\parallel}^t$ are respectively the complex amplitudes of

the incident, reflected, and transmitted electric field. Substituting in for $\bar{k}_i, \bar{k}_r, \bar{k}_t$, and \bar{r} , the electromagnetic fields are given by

$$\bar{E}_{i\parallel}(z) = E_{0\parallel}^i (\hat{x} \cos \theta_i + \hat{z} \sin \theta_i) e^{jk_1[x \sin \theta_i - z \cos \theta_i] - j\omega t} \quad (3.20)$$

$$\bar{E}_{r\parallel}(z) = -E_{0\parallel}^r (\hat{x} \cos \theta_r - \hat{z} \sin \theta_r) e^{jk_1[x \sin \theta_r + z \cos \theta_r] - j\omega t} \quad (3.21)$$

$$\bar{E}_{t\parallel}(z) = E_{0\parallel}^t (\hat{x} \cos \theta_t + \hat{z} \sin \theta_t) e^{jk_2[x \sin \theta_t - z \cos \theta_t] - j\omega t} \quad (3.22)$$

Given that $\nabla \times \bar{E} = j\omega\mu\bar{H}$, magnetic fields for parallel-polarized wave yield expressions

$$\bar{H}_{i\parallel}(z) = -\hat{y} \frac{E_{0\parallel}^i}{\eta_1} e^{jk_1[x \sin \theta_i - z \cos \theta_i] - j\omega t} \quad (3.23)$$

$$\bar{H}_{r\parallel}(z) = -\hat{y} \frac{E_{0\parallel}^r}{\eta_1} e^{jk_1[x \sin \theta_r + z \cos \theta_r] - j\omega t} \quad (3.24)$$

$$\bar{H}_{t\parallel}(z) = -\hat{y} \frac{E_{0\parallel}^t}{\eta_2} e^{jk_2[x \sin \theta_t - z \cos \theta_t] - j\omega t} \quad (3.25)$$

where η_1 and η_2 are intrinsic impedances for medium 1 and medium 2 respectively.

The intrinsic impedance is defined as $\eta_i = \sqrt{\frac{\mu_i}{\epsilon_i}}$ for $i = 1, 2$.

Total electric field for parallel polarization in medium 1 is the sum of incident and reflected parallel-polarized electric field waves, and total parallel-polarized electric field in medium 2 is equal to the parallel-polarized transmitted electric field.

$$\bar{E}_{1\parallel}(z) = \bar{E}_{i\parallel}(z) + \bar{E}_{r\parallel}(z) \quad (3.26)$$

$$\bar{E}_{2\parallel}(z) = \bar{E}_{t\parallel}(z) \quad (3.27)$$

At the boundary ($z = 0$), the tangential components of the electric and magnetic fields are continuous.

$$\bar{E}_{1\parallel}(0) \cdot \hat{x} = \bar{E}_{2\parallel}(0) \cdot \hat{x} \quad (3.28)$$

The following expression is obtained upon using Eqns (3.17), (3.18), (3.19), and applying the continuity condition on the tangential components of the electric field at $z = 0$.

$$E_{0\parallel}^i \left(\cos \theta_i e^{j(k_1 x \sin \theta_i - \omega t)} - \Gamma_{\parallel} \cos \theta_r e^{j(k_1 x \sin \theta_r - \omega t)} \right) = E_{0\parallel}^i \tau_{\parallel} \cos \theta_t e^{j(k_2 x \sin \theta_t - \omega t)} \quad (3.29a)$$

where $\Gamma_{\parallel} = E_{0\parallel}^r/E_{0\parallel}^i$ and $\tau_{\parallel} = E_{0\parallel}^t/E_{0\parallel}^i$. The magnetic field in medium 1 is defined as a sum of incident and reflected parallel-polarized magnetic field components. The total magnetic field in medium two is characterized only by transmitted parallel-polarized magnetic field. Applying the continuity condition on the tangential component of the magnetic field at the interface yields

$$\frac{E_{0\parallel}^i}{\eta_1} \left(e^{j(k_1 x \sin \theta_i - \omega t)} + \Gamma_{\parallel} e^{j(k_1 x \sin \theta_r - \omega t)} \right) = \frac{E_{0\parallel}^i}{\eta_2} \tau_{\parallel} e^{j(k_2 x \sin \theta_t - \omega t)} \quad (3.29b)$$

By Snell's law

$$k_1 \sin \theta_i = k_1 \sin \theta_r = k_2 \sin \theta_t \quad (3.29c)$$

Using Eqns (3.29a-c) the reflection and transmission coefficients of parallel polarization yield following expressions

$$\Gamma_{\parallel} = \frac{\eta_1 \cos \theta_i - \eta_2 \cos \theta_t}{\eta_1 \cos \theta_i + \eta_2 \cos \theta_t} \quad (3.30)$$

$$\tau_{\parallel} = \frac{2\eta_2 \cos \theta_i}{\eta_1 \cos \theta_i + \eta_2 \cos \theta_t} \quad (3.31)$$

3.4 Perpendicular Polarization

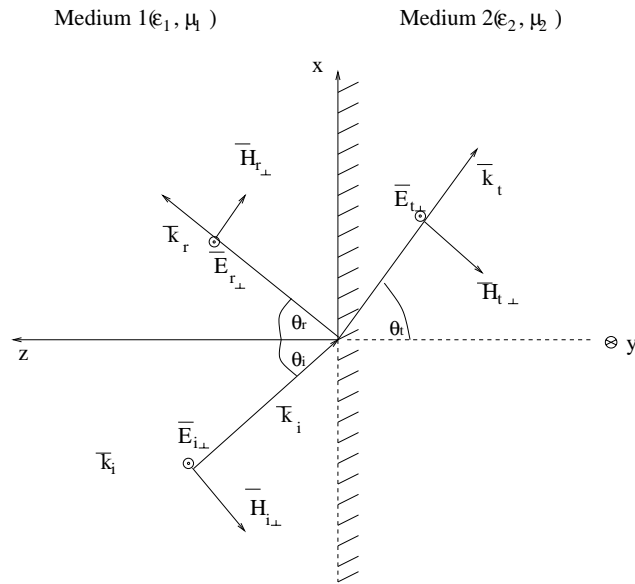


Figure 3.4. Perpendicular-polarized plane wave incident at an angle θ_i upon planar boundary

Previously it was said that any polarized wave can be decomposed by using superposition. If the same incident, reflected and transmitted waves (Eqns (3.14)-(3.16)) are used as in the parallel polarization analysis, it can be seen from Figure 3.4 that perpendicular polarization electric fields are perpendicular to the incident plane of propagation, and associated magnetic fields are parallel to same plane. Furthermore, the condition that $\vec{E}_{i\perp} \times \vec{H}_{i\perp}$ is collinear with \vec{k}_i .

The geometry used is detailed in Figure 3.4. Equating the tangential

components of the electric and magnetic field at the interface $z = 0$ yields.

$$E_{0\perp}^i \left(e^{jk_1 x \sin \theta_i} + \Gamma_{\perp} e^{jk_1 x \sin \theta_r} \right) = E_{0\perp}^i \tau_{\perp} e^{jk_2 x \sin \theta_t} \quad (3.32a)$$

$$\frac{E_{0\perp}^i}{\eta_1} \left(-\cos \theta_i e^{jk_1 x \sin \theta_i} + \cos \theta_r \Gamma_{\perp} e^{jk_1 x \sin \theta_r} \right) = -\frac{E_{0\perp}^i}{\eta_2} \tau_{\perp} \cos \theta_t e^{jk_2 x \sin \theta_t} \quad (3.32b)$$

where $\Gamma_{\perp} = E_{0\perp}^r/E_{0\perp}^i$ and $\tau_{\perp} = E_{0\perp}^t/E_{0\perp}^i$. By Snell's law

$$k_1 \sin \theta_i = k_1 \sin \theta_r = k_2 \sin \theta_t \quad (3.32c)$$

Solving Eqns (3.32a-c) for the reflection and transmission coefficients of perpendicular polarization yields following expressions

$$\Gamma_{\perp} = \frac{\eta_2 \cos \theta_i - \eta_1 \cos \theta_t}{\eta_1 \cos \theta_t + \eta_2 \cos \theta_i} \quad (3.33)$$

$$\tau_{\perp} = \frac{2\eta_2 \cos \theta_i}{\eta_1 \cos \theta_t + \eta_2 \cos \theta_i} \quad (3.34)$$

For the case where medium 1 is the air and medium 2 is sea water the relative permittivity $\epsilon = \epsilon_2/\epsilon_1$ is 72, whereas as the relative magnetic susceptibility $\mu = \mu_2/\mu_1$ is equal to one. The reflection coefficients for both polarizations are

shown in Figure 3.5.

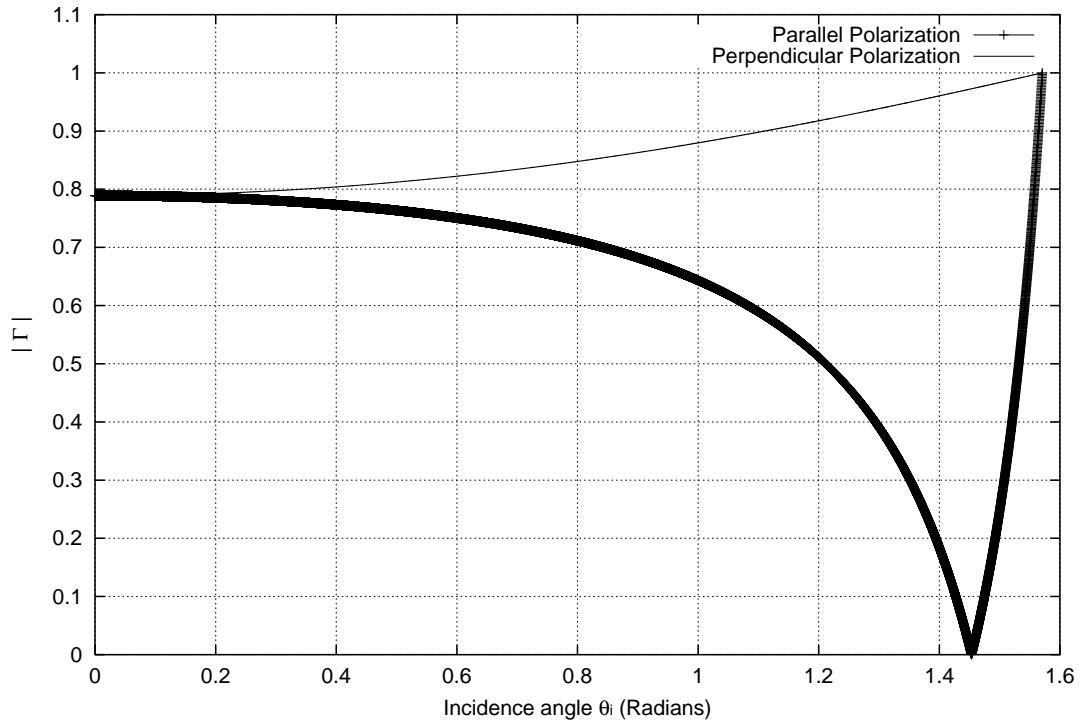


Figure 3.5. Parallel and perpendicular polarization reflection coefficients versus the angle of incidence, $\epsilon = 72$, $\mu = 1$

When incidence angle, θ_i , is zero, parallel and perpendicular reflection coefficients are equal in magnitude. At normal incidence the incident angle is zero, $\theta_i = 0$, and therefore, two reflection coefficients match as expected. On the other hand, at grazing incidence when $\theta_i = \frac{\pi}{2}$ the magnitude of both reflection coefficients are

equal to 1. Hence the wave is fully reflected. For non-magnetic materials, when parallel reflection coefficient is equal to 0, the angle of incidence is called Brewster's angle. At Brewster's angle the entire parallel-polarized component of the incidence wave is transmitted into medium 2. However, perpendicular-polarized component is not zero. Brewster's angle is also called polarizing angle due to the fact that the parallel-polarized component is fully transmitted into second medium, and perpendicularly-polarized component of the incident wave is reflected by the surface. Hence, the reflection process acts as a polarizer.

Reflected and transmitted angles can be expressed in terms of angle of incidence by Snell's laws

$$\Gamma_{\perp} = \frac{\eta_2 \cos \theta_i - \eta_1 \alpha}{\eta_2 \cos \theta_i + \eta_1 \alpha} \quad (3.35)$$

$$\Gamma_{\parallel} = \frac{\eta_1 \cos \theta_i - \eta_2 \alpha}{\eta_1 \cos \theta_i + \eta_2 \alpha} \quad (3.36)$$

where, $\alpha = \frac{\sqrt{k_2^2 - k_1^2 \sin^2 \theta_i}}{k_2}$.

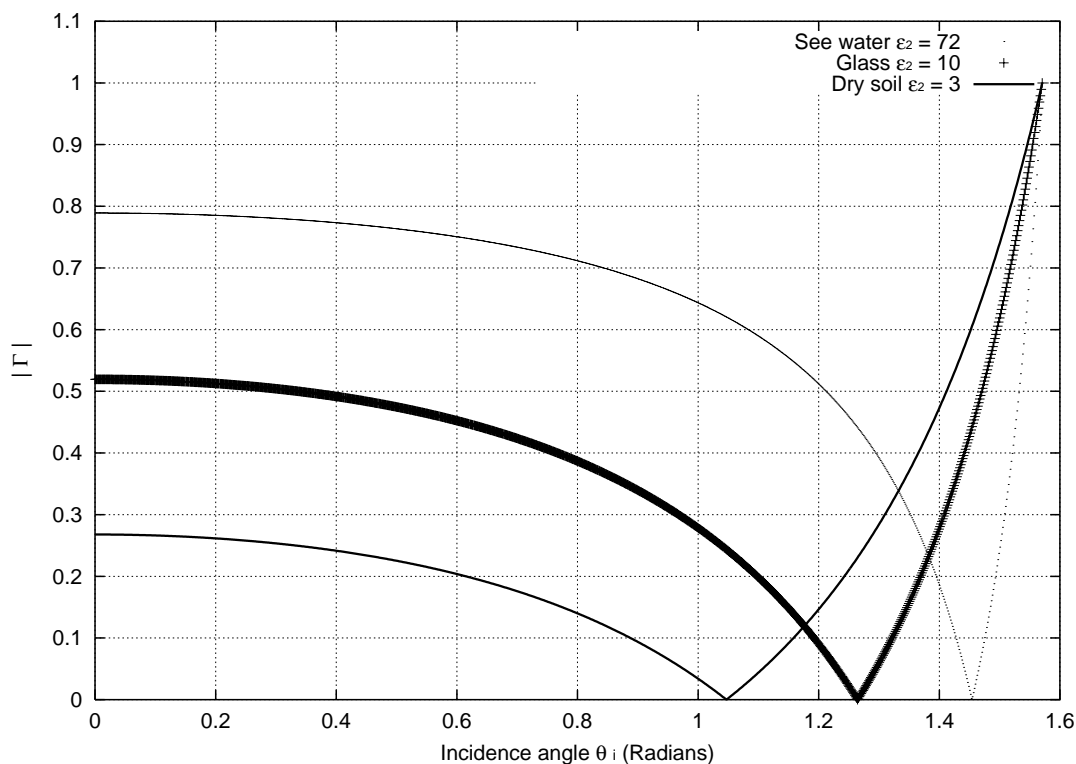


Figure 3.6. Absolute value of the parallel-polarized reflection coefficient as a function of θ_i for sea water, glass, and dry soil surface

Reflection coefficient demonstrates angular variations for different types of medium. Figure 3.6 shows angular variation of the parallel-polarized reflection coefficient for an incident wave coming from air onto three different dielectric surfaces: sea water ($\epsilon = 72$), glass ($\epsilon = 10$), and dry soil ($\epsilon = 3$). The relative electric permittivity of concrete wall is approximately equal to the electric

permittivity of the dry soil, therefore, further analysis will be done with $\varepsilon = 3$.

3.5 Inverse Laplace Transform of the Reflection Coefficient

For ease in our analysis a substitution is introduced into the previously derived reflection coefficients for both polarizations. The normalized variable q will be defined as

$$q = \frac{\cos \theta_i}{\sqrt{\mu\varepsilon - 1}} \quad (3.37)$$

where μ is relative magnetic permeability defined as the ratio of two mediums' magnetic permeabilities, $\mu = \frac{\mu_2}{\mu_1}$, and ε is relative electric permittivity defined as the ratio of two mediums' electric permittivities, $\varepsilon = \frac{\varepsilon_2}{\varepsilon_1}$. Applying these substitutions the obtained relations for reflection coefficients are as follows (Eqns (3.38) and (3.39))

$$\Gamma_{\parallel}(q) = \frac{\varepsilon q - \sqrt{1 + q^2}}{\varepsilon q + \sqrt{1 + q^2}} \quad (3.38)$$

$$\Gamma_{\perp}(q) = \frac{\sqrt{1+q^2} - \mu q}{\sqrt{1+q^2} + \mu q} \quad (3.39)$$

Parallel-polarized reflection coefficient, $\Gamma_{\parallel}(q)$, was chosen for further analysis of Laplace transform. Reflection coefficient $\Gamma_{\parallel}(q)$ can be represented in the following form

$$\begin{aligned} \Gamma_{\parallel}(q) &= \left\{ \lim_{q \rightarrow \infty} \Gamma_{\parallel}(q) \right\} + R(q) \\ &= \frac{\varepsilon - 1}{\varepsilon + 1} + \frac{\varepsilon}{\varepsilon^2 - 1} \frac{\left(q - \sqrt{1+q^2} \right)^2 - \frac{\varepsilon - 1}{\varepsilon + 1}}{q^2 - \frac{1}{\varepsilon^2 - 1}} \end{aligned} \quad (3.40)$$

Since $\lim_{q \rightarrow \infty} \Gamma_{\parallel}(q)$ is $\frac{\varepsilon - 1}{\varepsilon + 1}$, $R(q)$ is then defined as

$$R(q) = \frac{\varepsilon}{\varepsilon^2 - 1} \frac{\left(q - \sqrt{1+q^2} \right)^2 - \frac{\varepsilon - 1}{\varepsilon + 1}}{q^2 - \frac{1}{\varepsilon^2 - 1}} \quad (3.41)$$

The function $R(q)$ depends on the parameter ε . Figure 3.7 depicts the absolute

value of $R(q)$ and its variation with different values of ε , where ε is taken as complex value.

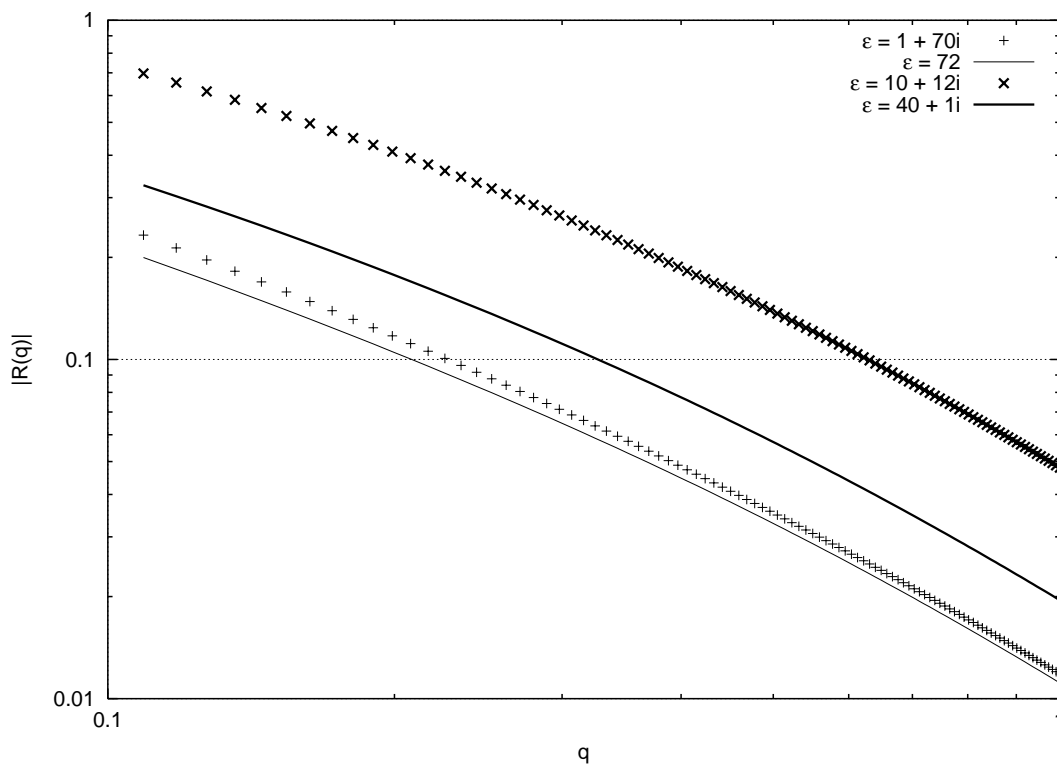


Figure 3.7. The absolute value of $R(q)$ varying with different values of parameter ε

The reflection coefficient will be represented as Laplace transform integral of an unknown function $S_{||}(p)$.

$$\Gamma_{\parallel}(q) = \int_0^{\infty} S_{\parallel}(p) e^{-pq} dq \quad (3.42)$$

where $S_{\parallel}(p)$ is to be determined through the further analysis. From Eqn (3.42), $S_{\parallel}(p)$ can be expressed as the inverse Laplace formulation of $\Gamma_{\parallel}(q)$

$$S_{\parallel}(p) = \frac{1}{2\pi j} \int_{-j\infty+c}^{j\infty+c} \Gamma_{\parallel}(q) e^{pq} dq \quad (3.43)$$

Combining Eqns (3.40) and (3.43), $S_{\parallel}(p)$ is defined through the relation

$$S_{\parallel}(p) = \frac{\varepsilon - 1}{\varepsilon + 1} \delta(p) + \frac{1}{2\pi j} \int_{-j\infty+c}^{j\infty+c} R(q) e^{pq} dq \quad (3.44)$$

In evaluating complex integrals, it is essential to examine all singularities of the integrand. The singularities of the function $R(q)$ exist at points where $R(q)$ is not analytic. From the expression for $R(q)$ it can be seen that there are two possible poles and two branch points. Two possible poles occur at $q = \pm a$ where $a = \frac{1}{\sqrt{\varepsilon^2 - 1}}$. A key element in the analysis is the selection of the sign of the term $\sqrt{1 + q^2}$. When the real part of q is positive, the positive branch will be chosen.

Otherwise the negative branch will be used.

As q approaches a one can write

$$q - \sqrt{1 + q^2} = (x + a) - \left\{ \sqrt{1 + a^2} \right\} \sqrt{1 + \frac{x(x + 2a)}{1 + a^2}} \quad (3.45)$$

where $q - a = x$. Letting $a = 1/\sqrt{\varepsilon^2 - 1}$ the term $\sqrt{1 + a^2} = \varepsilon/\sqrt{\varepsilon^2 - 1}$. Taking the Taylor series about $x = 0$ of the numerator of $R(q)$ yields

$$\lim_{x \rightarrow +a} \left(q - \sqrt{1 + q^2} \right)^2 - \frac{\varepsilon - 1}{\varepsilon + 1} = -2 \frac{(\varepsilon - 1)^2}{\varepsilon \sqrt{\varepsilon^2 - 1}} (q - a) + O((q - a)^2) \quad (3.46)$$

Since the leading term is multiplied by $(q - a)$ a pole-zero cancellation occurs. The function is analytic for $q = 1/\sqrt{\varepsilon^2 - 1}$.

For $q = -a$ the term $\sqrt{1 + a^2} = -\varepsilon/\sqrt{\varepsilon^2 - 1}$. Taking the Taylor series about $x = 0$ of the numerator of $R(q)$ yields

$$\lim_{x \rightarrow -a} \left(q - \sqrt{1 + q^2} \right)^2 - \frac{\varepsilon - 1}{\varepsilon + 1} = 2 \frac{(\varepsilon - 1)^2}{\varepsilon \sqrt{\varepsilon^2 - 1}} (q + a) + O((q + a)^2) \quad (3.47)$$

Since the leading term is multiplied by $(q + a)$ a pole-zero cancellation occurs.

Hence the function is analytic for $q = -1/\sqrt{\varepsilon^2 - 1}$.

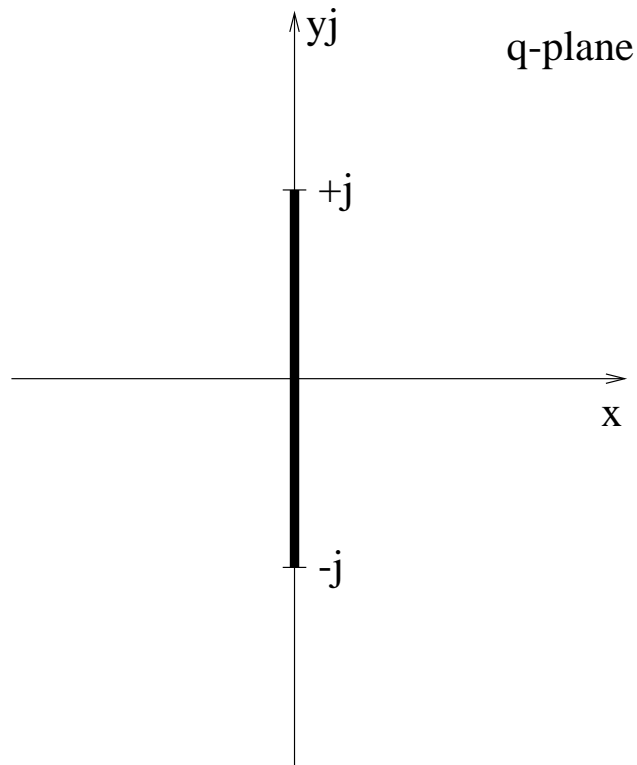


Figure 3.8. Definitions of branch line for $R(q)$

In the given problem poles are canceled by zeroes as in the expression at

$q = \pm \sqrt{\frac{1}{\varepsilon^2 - 1}}$ and have no effect on the solution. However, the effect of the

branch point has to be taken into account. $R(q)$ is double-valued function, and has

the same branch points $\pm j$ as the function $\sqrt{1+q^2}$. Given that $q = x + jy$ the branch line can be defined as $x = 0$ and $-1 \leq y \leq 1$ and is shown in Figure 3.8.

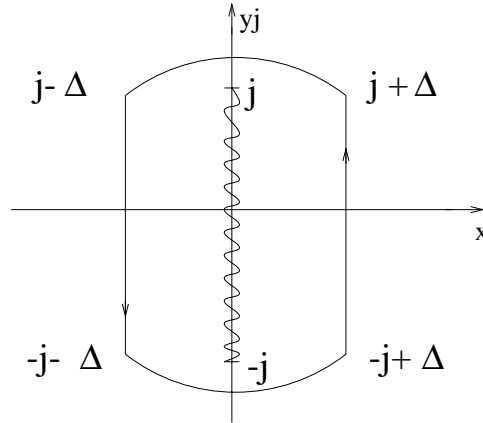


Figure 3.9. Branch points and branch line for $R(q)$

Assuming that branch line is defined between two branch points (Figure 3.9), the two branch points yield the following expression

$$S_{\parallel}(p) = \frac{\varepsilon - 1}{\varepsilon + 1} \delta(p) + \frac{1}{2\pi j} \left[\int_{-j+\Delta}^{+j+\Delta} F(q)e^{pq} dq + \int_{+j-\Delta}^{-j-\Delta} F(q)e^{pq} dq \right] \quad (3.48)$$

where,

$$F(q) = \left[\frac{\varepsilon}{1 - \varepsilon^2} \right] \frac{2q\sqrt{1 + q^2}}{q^2 - \frac{1}{\varepsilon^2 - 1}} \quad (3.49)$$

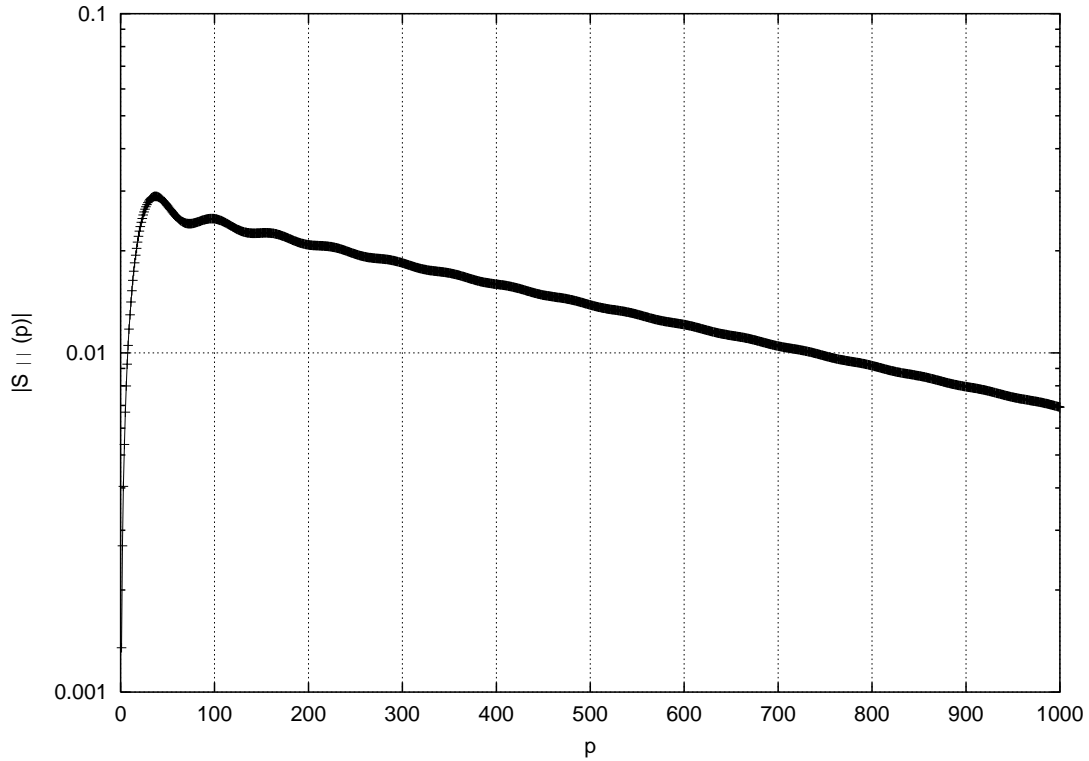


Figure 3.10. Numerical solution for $S_{||}(p) - \left(\frac{\varepsilon - 1}{\varepsilon + 1} \right) \delta(p)$ for water ($\varepsilon = 72$).

$F(q)$ actually represents the first term of $R(q)$ (Eqn (3.41)) and it has the only contribution to the image source. Introducing yet another substitution, $q = jy$, the

expression for $S_{||}(p)$ is

$$S_{||}(p) = \frac{\varepsilon - 1}{\varepsilon + 1} \delta(p) - \frac{\varepsilon}{\varepsilon^2 - 1} \frac{4}{\pi} \int_0^1 \frac{y\sqrt{1-y^2}}{y^2 + \frac{1}{\varepsilon^2 - 1}} \sin(py) dy \quad (3.50)$$

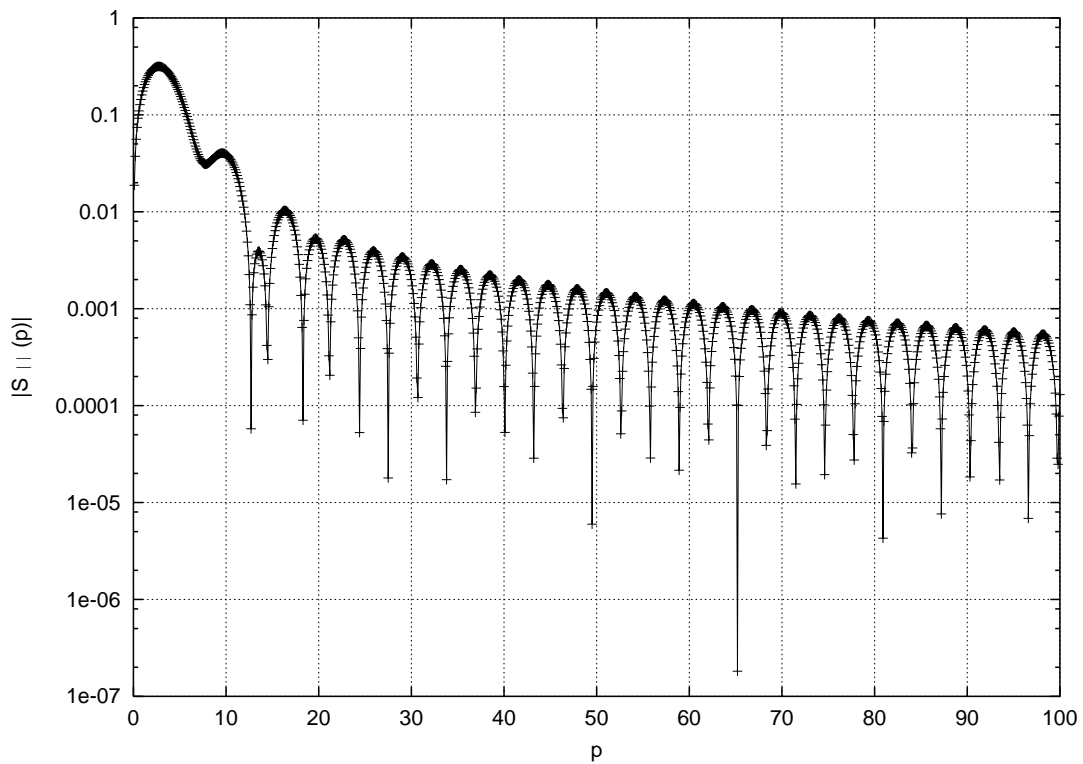


Figure 3.11. Numerical solution for $S_{||}(p) - \left(\frac{\varepsilon - 1}{\varepsilon + 1}\right)\delta(p)$ for dry soil ($\varepsilon = 3$).

We are interested in the indoor case where one of the reflection cases that can occur is when the wave travels from air onto wall. The expression for $S_{\parallel}(p)$ (Eqn (3.50)) can be solved numerically for the mentioned case (Figure 3.10 and Figure 3.11).

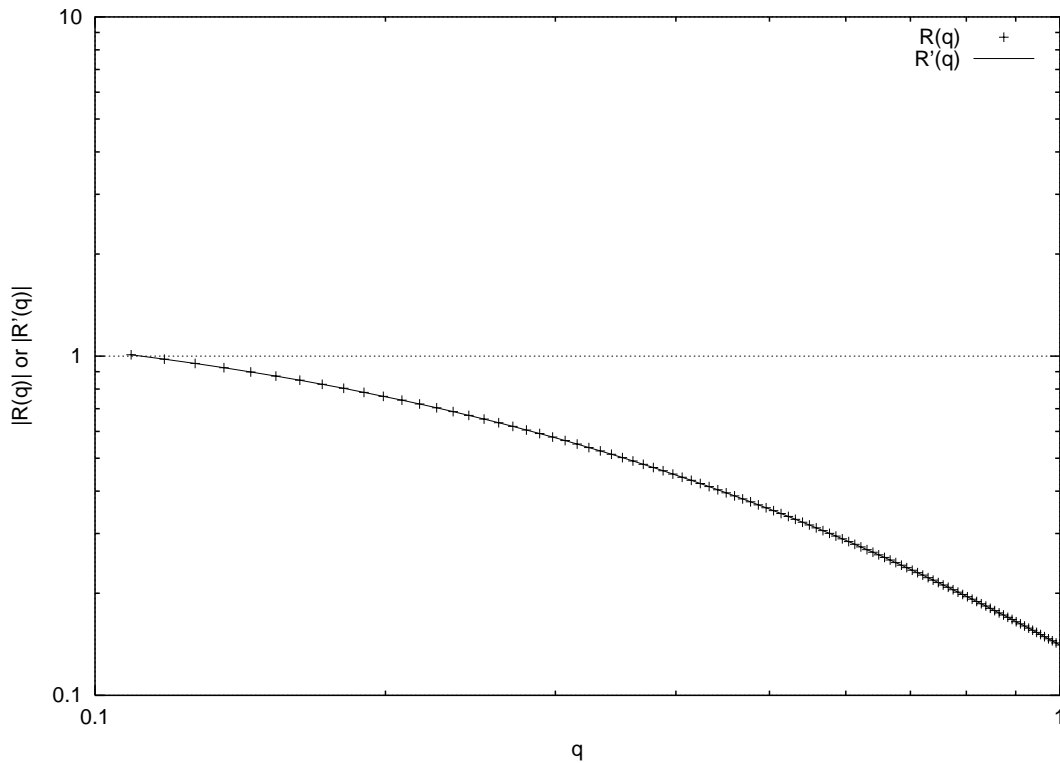


Figure 3.12. Absolute value of $R(q)$ and $R'(q) - \left(\frac{\varepsilon - 1}{\varepsilon + 1}\right)$ ($\varepsilon = 3$).

It can be seen from both graphs that $S_{\parallel}(p)$ decreases inversely with p , and it

decreases exponentially. In Figure 3.10 $S_{\parallel}(p)$ is numerically solved for the wave traveling from air onto the water, and in Figure 3.11 for the wave traveling from air onto to dry soil.

In order to show that the proper branch point was selected in evaluation of the reflection coefficient, the Laplace transform was taken of $S_{\parallel}(p)$

$$R'(q) = \int_0^{\infty} S_{\parallel}(p) e^{-qp} dp \quad (3.51)$$

In Figure 3.12 $R(q)$ and $R'(q)$ are matching, which demonstrates that image source, $F(q)$, along with the branch points were chosen accurately.

3.6 *Radiated Field*

Given that magnetic and electric fields are continuous across the boundary between two mediums, boundary can be substituted with a point source. A point source is considered as shown in Figure 3.13, where point source is located at coordinates $(x, y, z) = (0, 0, z_s)$.

The total reflected field is defined as

$$\Pi(r, \theta_i, k_1) = \int_0^\infty \frac{S_{\parallel}(p)e^{jk_1\psi}}{\psi} dp \quad (3.52)$$

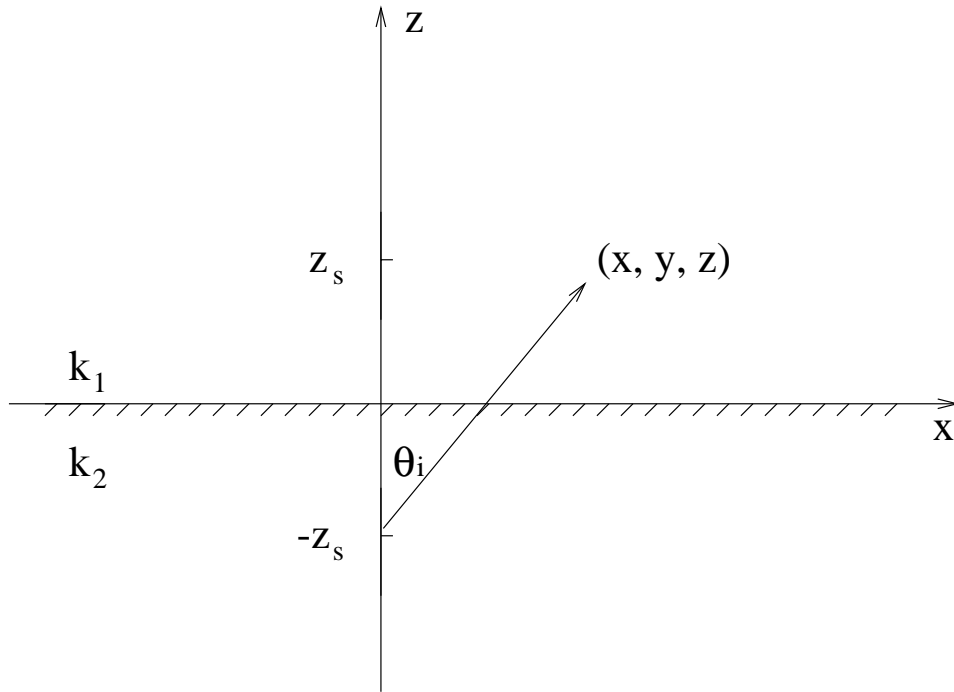


Figure 3.13. The point source located at $(0, 0, z_s)$, receiver located at (x, y, z) , and image source is located at $(0, 0, -z_s - \frac{jp}{k_1\sqrt{\mu\epsilon - 1}})$.

The corresponding image source is located in the complex plane at $(0, 0, -$

$z_s - \frac{jp}{k_1\sqrt{\mu\epsilon - 1}}$), therefore, ψ is defined as

$$\psi = \sqrt{x^2 + y^2 + \left(z + z_s + \frac{jp}{k_1 \sqrt{\mu\epsilon - 1}}\right)^2} \quad (3.53)$$

where $x^2 + y^2$ is horizontal distance between source and receiver, because x_s and y_s are zero. If distance between the image source and receiver is defined as r , then

$$r^2 = x^2 + y^2 + (z + z_s)^2 \quad (3.54)$$

Considering the normalizing factor previously used (Eqn (3.37)) and distance r (Eqn (3.54)), ψ can be simplified to the following expression

$$\psi = r \sqrt{1 + \frac{2jp}{rk_1} \frac{\cos \theta_i}{\sqrt{\mu\epsilon - 1}} - \left(\frac{p}{rk_1 \sqrt{\mu\epsilon - 1}}\right)^2} \quad (3.55)$$

The first term of $S_{\parallel}(p)$ (Eqn (3.50)) is a delta function which is zero at $p \leq 0$.

Therefore, the total field of the image source can be rewritten as

$$\Pi(r, k) = \frac{e^{jk_1 r}}{r} \left[\frac{\epsilon - 1}{\epsilon + 1} + \int_0^{\infty} Ss(p) \frac{e^{jk_1 r \left(\frac{\psi}{r} - 1\right)}}{\frac{\psi}{r}} dp \right] \quad (3.56)$$

where $Ss(p)$ is the second term of $S_{\parallel}(p)$,

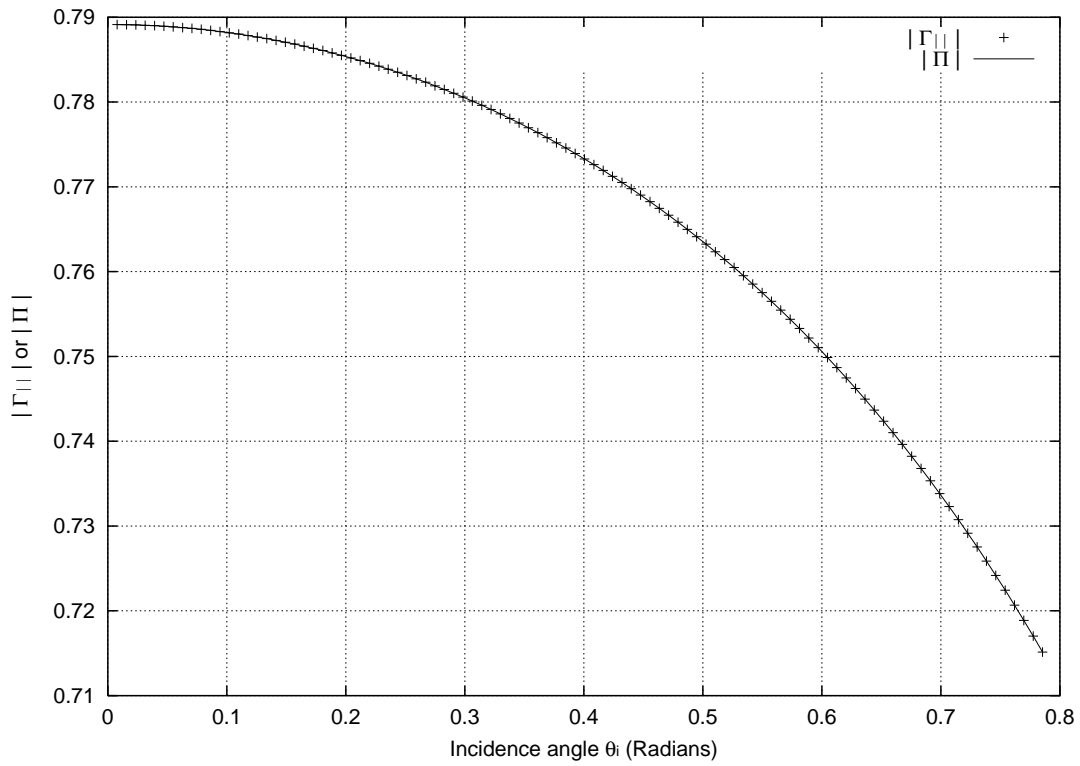


Figure 3.14. Parallel-polarized reflection coefficient, Γ , versus the total field, $\Pi \frac{r}{e^{jk_1 r}}$, when $k_1 r = 100,000$ and $\varepsilon = 72$

$$Ss(p) = -\frac{\varepsilon}{\varepsilon^2 - 1} \frac{4}{\pi} \int_0^1 \frac{y\sqrt{1-y^2}}{y^2 + \frac{1}{\varepsilon^2 - 1}} \sin(py) dy \quad (3.57)$$

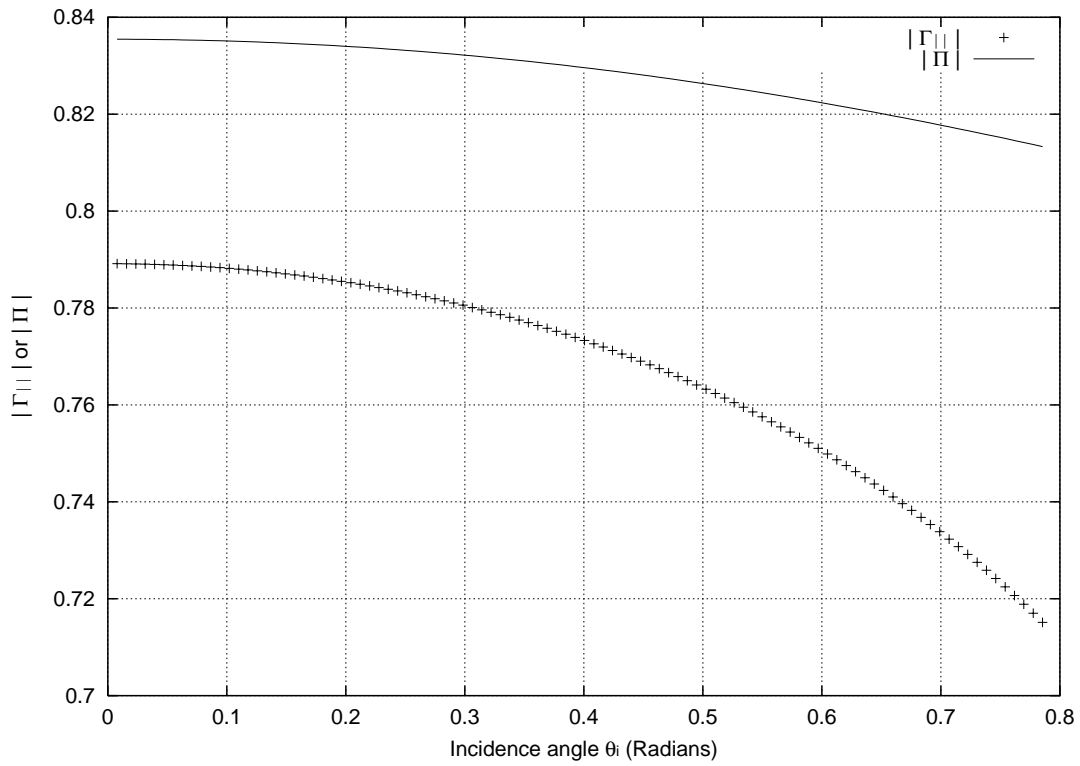


Figure 3.15. Parallel-polarized reflection coefficient, Γ , versus the total field, $\Pi \frac{r}{e^{jk_1 r}}$, when $k_1 r = 100$ and $\varepsilon = 72$

Detailed derivation of the entire reflected field is presented in Appendix A. The solution can be easily evaluated using numerical methods. From Figures 3.14 and 3.15 it can be seen that the total field, Π , depends on the value of $k_1 r$, where k_1 is the wavenumber. For the large values of $k_1 r$, reflection coefficient and the total field match well (Figure 3.14).

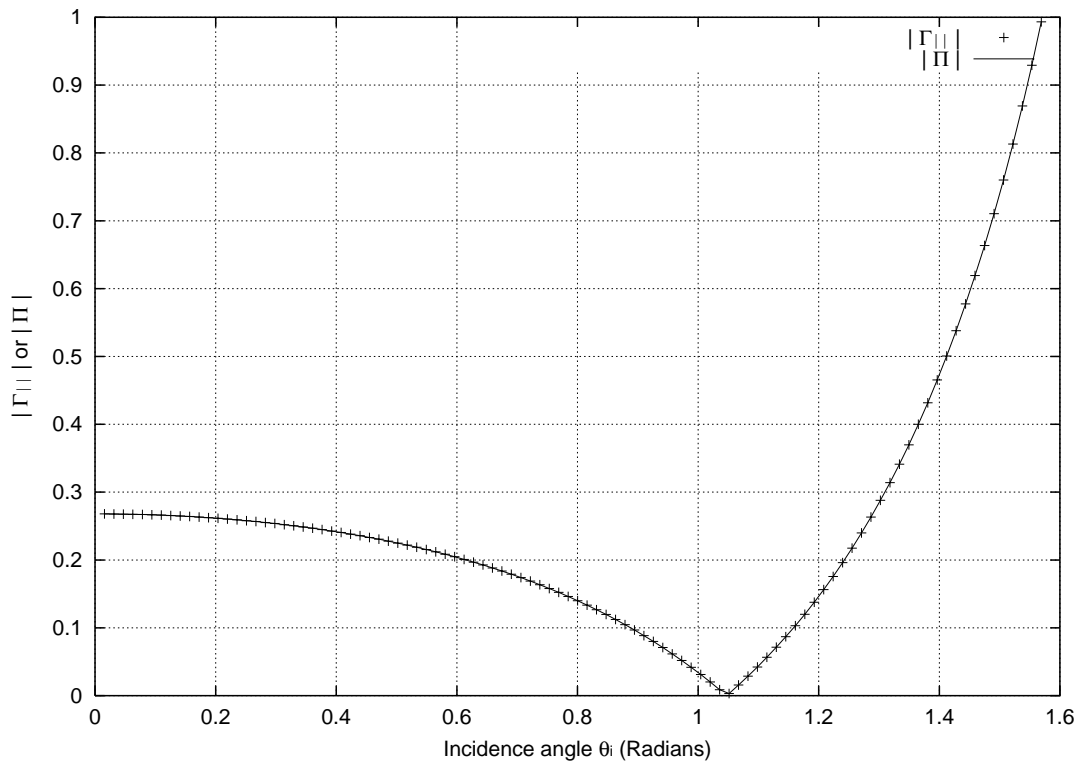


Figure 3.16. Parallel-polarized reflection coefficient, Γ , versus the total field, $\Pi \frac{r}{e^{jk_1 r}}$, when $k_1 r = 100,000$ and $\varepsilon = 3$

However, the field does not only depend on the $k_1 r$ value, or frequency and distance between the image source and receiver. It also depends on the electric permittivity, ε . Figures 3.14 and 3.15 represent the field for the wave which travels from air onto the sea water. Furthermore, Figures 3.16 and 3.17 represent the wave traveling from air onto dry soil, or the wall in this case.

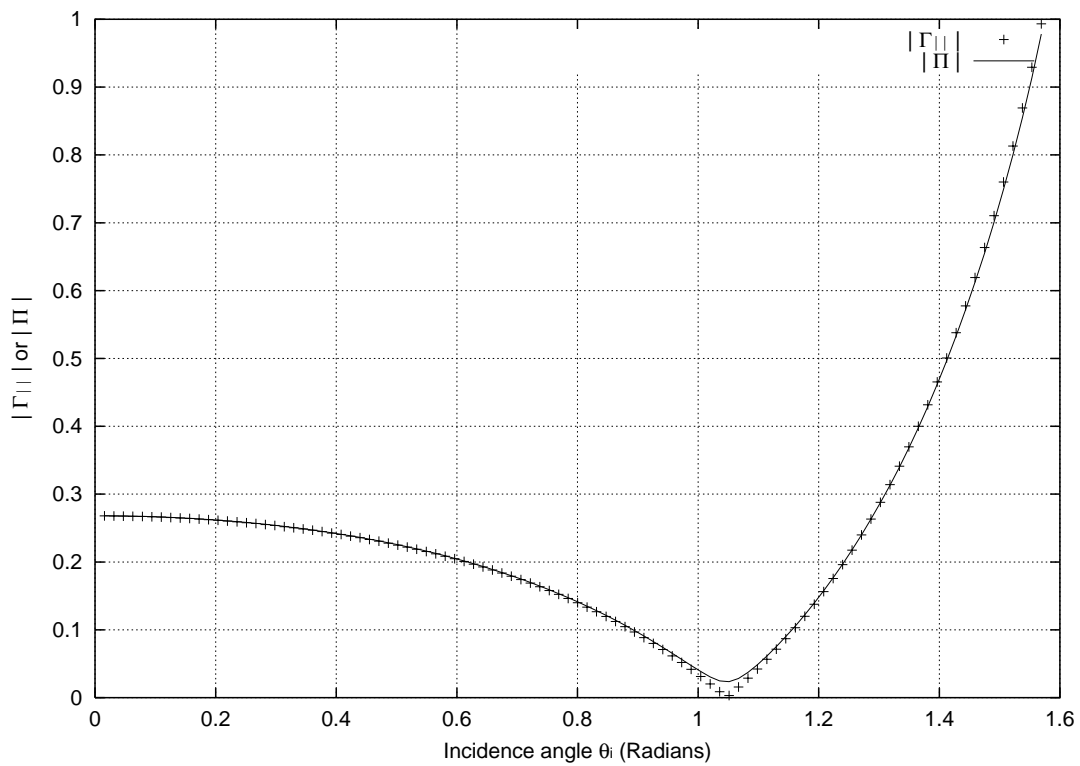


Figure 3.17. Parallel-polarized reflection coefficient, Γ , versus the total field, $\Pi \frac{r}{e^{jk_1 r}}$, when $k_1 r = 100$ and $\varepsilon = 3$

It appears that for the smaller values ε the field is likely to behave more like reflection coefficient.

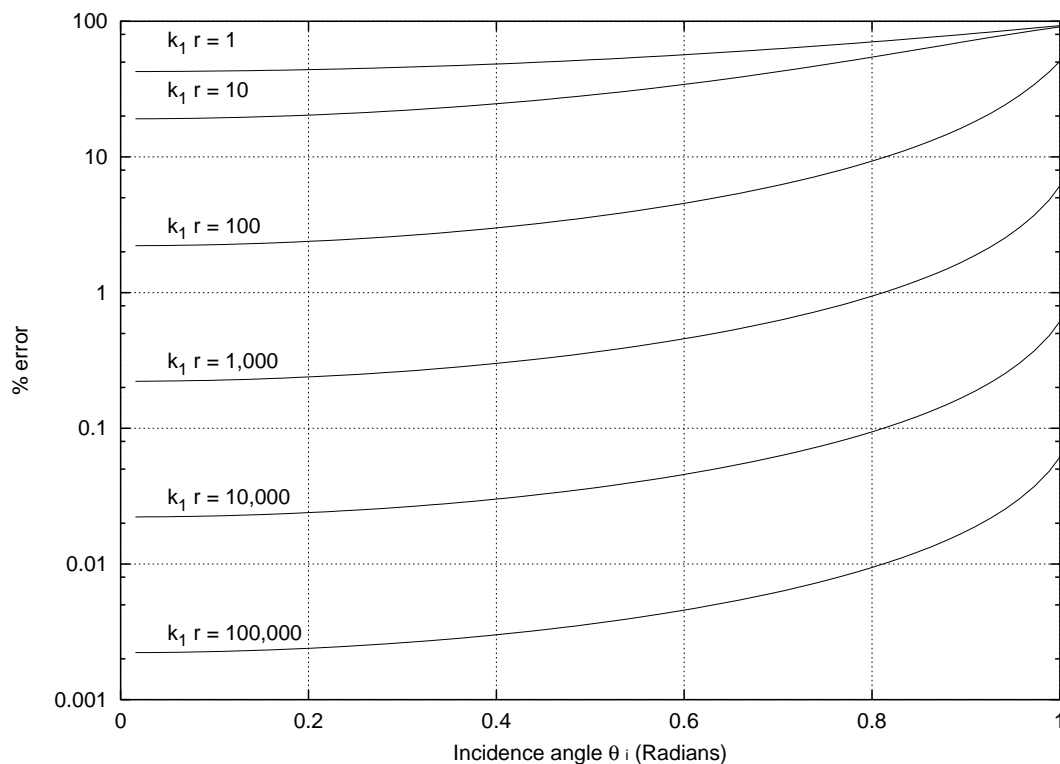


Figure 3.18. Error for different values of $k_1 r$ when $\varepsilon = 3$

However, Figure 3.14-3.17 show magnitudes of parallel-polarized reflection coefficient and total field. This does not provide complete picture of the fields behavior due to the phase change which is not shown on these graphs. In order to get better idea of the field's dependence on the values of $k_1 r$ and ε , error was found. Error represents the percent difference between the plane wave reflection coefficient and that obtained by the field calculation.

For very small value of $k_1 r$ error is larger for smaller values of ε (Figure 3.20). However, as the value of $k_1 r$ increases the error is inversely proportional to the $k_1 r$ value (Figures 3.18 and 3.19). Furthermore, for the smaller values ε error decreases faster.

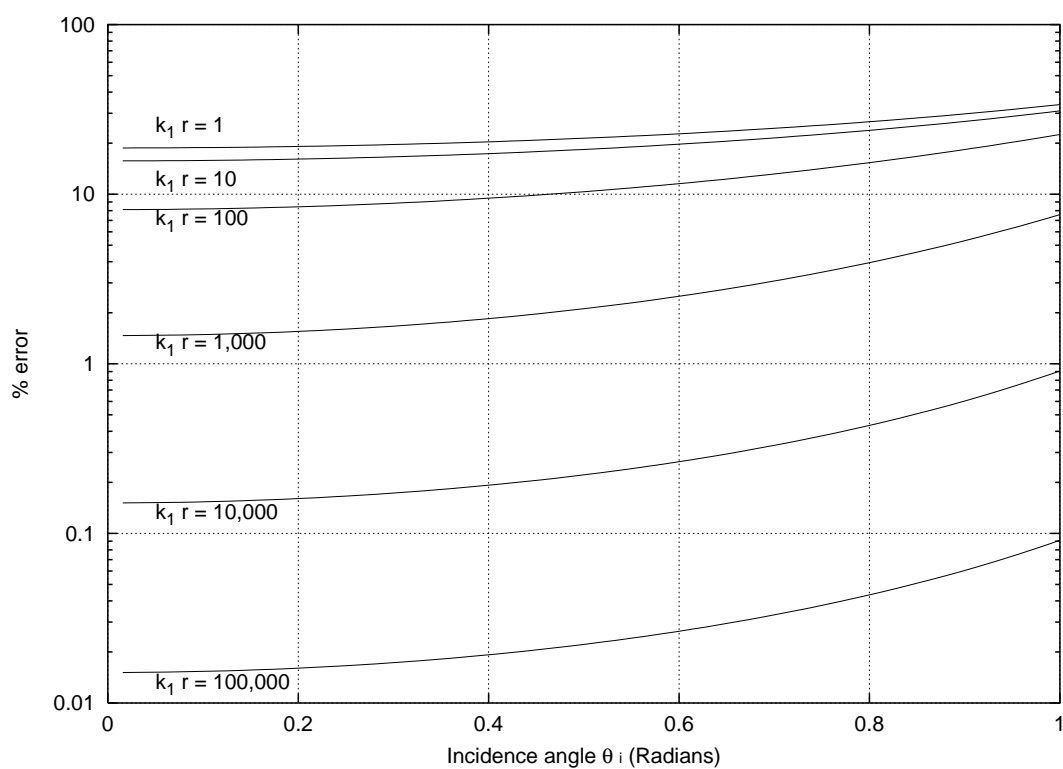


Figure 3.19. Magnitude of error for different values of $k_1 r$ when $\varepsilon = 72$

When the $k_1 r$ value is high that means that either distance from source to receiver

is large or that frequency is high, meaning that at large distances plane wave is good approximation for spherical wave. On the other hand, for the smaller values of $k_1 r$ reflection coefficient and the total field differ. Since we are looking into short-range reflection this result is of great significance for further analysis in obtaining the impulse response of the wave propagation.

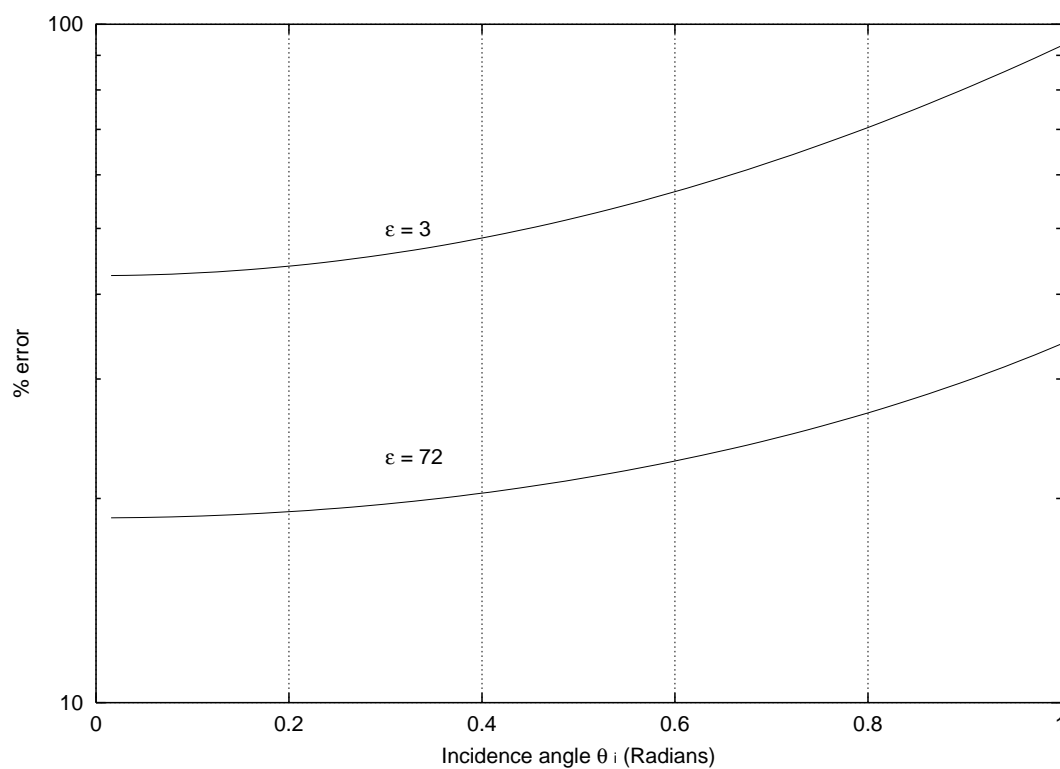


Figure 3.20. Magnitude of error when $k_1 r = 1$ for $\epsilon = 3$ and $\epsilon = 72$

As seen from aforementioned results, the signal is more likely to reflect at higher amplitudes, at low frequencies, and short distances. Hence, the point source acts like a low pass filter, and therefore, on the plane wave reflection coefficient the spectrum will shift. Due to the high reflection, once converted into time-domain, the pulse will spread. The problem can occur if the pulse spreads wider than a assigned frame time. In this case, pulse might be detected as noise, and it would be canceled out.

Chapter 4

INFLUENCE OF THE SHORT-TIME/RANGE REFLECTION ON THE UWB SIGNAL

4.1 Introduction

During UWB transmission, the UWB signal will be reflected from obstacles before reaching the receiver. Long-range reflections do not have high impact on the signal recovery. However, when the short-range reflections occur the pulse changes its original position. If the pulse shift is small the receiver may decode the signal with error during demodulation.

In previous chapters we described the principles used in signal modulation and demodulation, and determined the radiated field around the dipole antenna. PPM is a common method for modulation of UWB signal, as well as the matched filter and correlator that are used for demodulation. However, the short-range/time reflection in the channel through which UWB signal is propagating does not have a standard solution and it is still problematic in the UWB technology. In an indoor case, where the receiver will most likely be attached to the wall, the occurrence of short-range reflections is eminent. Prediction of the channel transfer function can be used to minimize the reflected wave's effects at the receiver.

In this chapter we will determine the channel impulse response consisting of a single reflection from a dielectric boundary. In particular we are interested in the short-range/time reflections that occur in indoor wireless transmission. Therefore, we will discuss the influence of the short-range reflection on the UWB signal.

4.2 *Time-domain Solution*

In this section we will present the time-domain solution of the radiated field from a dipole antenna using the results outlined in Chapter 3. This time-domain solution of the field can be used as an approximate model of the impulse response of the channel through which the UWB signal is sent. Given two mediums, it is assumed that within a channel only one short-range reflection occurs. Furthermore, the impulse response of the channel is considered to be time-invariant.

By knowing the features of the reflected signals that can occur within a channel one can significantly decrease the influence of the signal interference at the receiver. We are most interested in the closed environment case, and therefore, we will consider computing the radiated field for wave propagating from air onto the wall. In this case relative electric permittivity of the wall is $\varepsilon = 3$.

The reflected wave is observed at a distance r from the image source and angle θ_i measured relative to the normal of the boundary as shown in Figure 3.2.

Given that the source provides a time-harmonic excitation $e^{-j\omega t}$ to the medium, an outwardly traveling wave ensues with wavenumber $k_0 = \frac{\omega_0}{c_1}$. The amplitude of the z component of the Hertzian potential for this wave is given by

$$\Pi(\omega_0, r, \theta_i) = \left\{ \frac{e^{jk_0 r}}{4\pi r} \right\} A(\omega_0, r, \theta_i) \quad (4.1)$$

where,

$$A(\omega_0, r, \theta_i) = \int_0^\infty S_{\parallel}(p, \omega_0) \left[\frac{e^{jk_0 r \left(\frac{\psi}{r} - 1 \right)}}{\frac{\psi}{r}} \right] dp \quad (4.2)$$

and

$$\frac{\psi^2}{r^2} = 1 + \frac{j2p}{k_0 r} \frac{\cos \theta_i}{\sqrt{\mu\epsilon - 1}} - \left(\frac{p}{k_0 r \sqrt{\mu\epsilon - 1}} \right)^2 \quad (4.3)$$

The time-domain response can be obtained by applying the inverse Fourier transform to A in Eqn (4.1).

$$a(t, r, \theta_i) = \frac{1}{2\pi} \int_{-\infty}^{\infty} A(\omega_0, r, \theta_i) e^{-j\omega_0 t} d\omega_0 \quad (4.4)$$

The term $\left\{ \frac{e^{jk_0 r}}{4\pi r} \right\}$ in Eqn (4.1), offers a time delay $\frac{r}{c}$ and scales the aforementioned result by $\frac{1}{4\pi r}$. Hence, the time domain solution for the Hertzian potential of the reflected wave is

$$\pi_z(t, r, \theta_i) = \frac{a\left(t - \frac{r}{c}, r, \theta_i\right)}{4\pi r} \quad (4.5)$$

The inversion of the Fourier transform can be performed using the Fast Fourier transform after suitable nondimensionalizations and discretizations are performed on the complex amplitude A . The first step is to scale frequency and time with respect to the sampling frequency f_s . The nondimensional quantities are denoted by ' \sim '.

$$\omega_0 = \left[\frac{2\pi f_0}{f_s} \right] f_s = \tilde{\omega}_0 f_s \quad (4.6)$$

$$t = \tilde{t} \left[\frac{1}{f_s} \right] \quad (4.7)$$

The spatial variables will be nondimensionalized using the length scale $\frac{c}{f_s}$.

$$r = \tilde{r} \left[\frac{c}{f_s} \right] \quad (4.8)$$

When expressed in terms of the nondimensional parameters \tilde{t} , $\tilde{\omega}_0$, and \tilde{r} , A yields the following expression

$$A(\tilde{\omega}_0, \tilde{r}, \theta_i) = \int_0^{\infty} S_{||}(p, \tilde{\omega}_0 f_s) \left[\frac{e^{j\tilde{\omega}_0 \tilde{r} \left(\frac{\tilde{\psi}}{\tilde{r}} - 1 \right)}}{\frac{\tilde{\psi}}{\tilde{r}}} \right] dp \quad (4.9)$$

where,

$$\frac{\tilde{\psi}^2}{\tilde{r}^2} = 1 + \frac{j2p \cos \theta_i}{\tilde{\omega}_0 \tilde{r} \sqrt{\mu \epsilon} - 1} - \left(\frac{p}{\tilde{\omega}_0 \tilde{r} \sqrt{\mu \epsilon} - 1} \right)^2 \quad (4.10)$$

Therefore, the nondimensionalized expression for the time-domain solution of $A(\tilde{\omega}_0, \tilde{r}, \theta_i)$ becomes

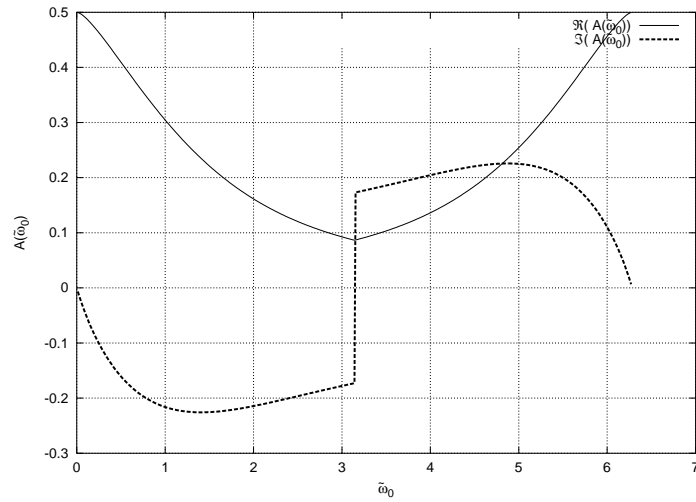
$$a(\tilde{t}, \tilde{r}, \theta_i) = \frac{1}{2\pi} \int_{-\infty}^{\infty} A(\tilde{\omega}_0, \tilde{r}, \theta_i) e^{-j\tilde{\omega}_0 \tilde{t}} d\tilde{\omega}_0 f_s \quad (4.11)$$

To obtain a discrete representation of Eqn (4.9), one equates $\tilde{\omega}_0 = \frac{2\pi k}{N}$ where k is the index of the frequency harmonic and N is equal to the number of frequency samples between 0 and f_s . The result is periodic in time and frequency. Hence, \tilde{t} takes on integral values between 0 and $N - 1$. The result is not periodic in space. So \tilde{r} can take on any value. Expressing $A(2\pi k/N, \tilde{t}, \theta_i) = A(k, \tilde{t}, \theta_i)$ in Eqn (4.9) yields the discrete Fourier transform

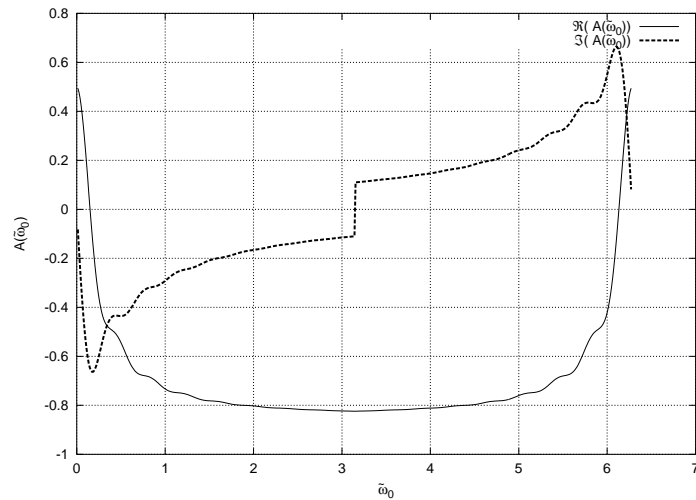
$$\tilde{a}(\tilde{t}, \tilde{r}, \theta_i) = \frac{a(\tilde{t}, \tilde{r}, \theta_i)}{f_s} = \frac{1}{N} \sum_{k=0}^{N-1} A(k, \tilde{t}, \theta_i) e^{-j\frac{2\pi k \tilde{t}}{N}} \quad (4.12)$$

Hence, \tilde{a} is the area of a in a $\frac{1}{f_s}$ in each sample time interval.

The FFT algorithm assumes that the signal is periodic. Each period of the signal consists of N points. Time-domain solution for the radiated field is a real valued signal. The resulting real valued time-domain signal can be achieved if its spectrum is conjugate symmetric. In other words, the second half of the signal needs to be the complex conjugate of the first part. Figure 4.1 shows complex amplitude A for $\varepsilon = 3$. Time-domain solution of $\tilde{a}(\tilde{t}, \tilde{r}, \theta_i)$ is shown in Figure 4.2.



(a)



(b)

Figure 4.1. The frequency response for complex amplitude A for (a) $\varepsilon = 3$,

$$\tilde{r} = 3.24, \theta_i = \frac{\pi}{3}, \text{ (b) } \varepsilon = 3, \tilde{r} = 40, \theta_i = 1.53 \text{ rad}$$

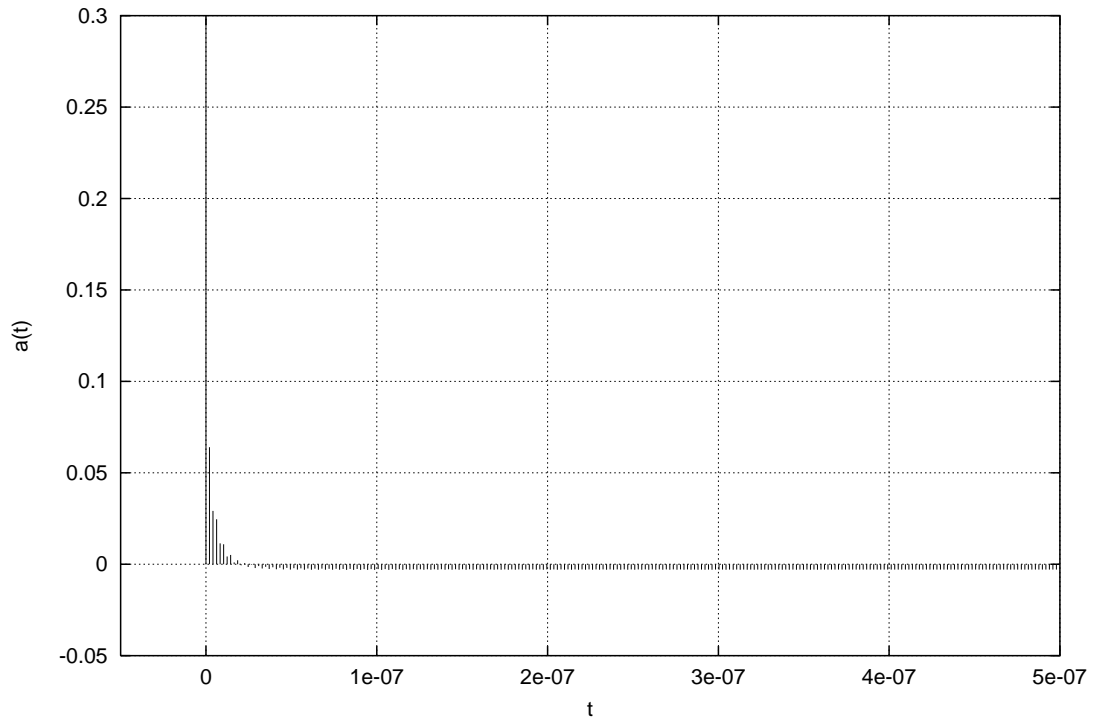


Figure 4.2. Time-domain impulse response of $a(t)$ for $\varepsilon = 3$, $\tilde{r} = 6.67$, $\theta = 0.24 \text{ rad}$

4.3 Relationship Between the Hertzian Potential and the Electric Field

In the previous analysis we assumed current which was harmonically time varying as $e^{-j\omega t}$. Given the wave equation

$$\left[\nabla^2 + \omega^2 \mu \varepsilon \right] \bar{\Pi} e^{-j\omega t} = -\hat{z} \frac{I_0 h}{-j\omega \varepsilon} \delta(\bar{x}) e^{-j\omega t} \quad (4.13)$$

For vertically directed dipole the solution for the z-component of the Hertzian potential is

$$\Pi_z = \frac{I_0 h}{-j\omega \varepsilon} \Pi \quad (4.14)$$

In spherical coordinates Hertzian potential can be presented as

$$\bar{\Pi} = \Pi_r \hat{r} + \Pi_\theta \hat{\theta} \quad (4.15)$$

where $\Pi_r = \Pi_z \cos \theta_i$, and $\Pi_\theta = -\Pi_z \sin \theta_i$. Electric field is proportional to the Hertzian potential. The relation between the two is described in the following expression

$$\bar{E} = \nabla(\nabla \bar{\Pi} + \omega^2 \varepsilon \mu \bar{\Pi}) \quad (4.16)$$

When one expands the aforementioned expression, the electric field yields following expressions

$$E_\theta = \frac{1}{r} \frac{\partial}{\partial \theta} \left[\frac{1}{r^2} \frac{\partial}{\partial r} (r^2 \Pi_r) + \frac{1}{r \sin \theta_i} \frac{\partial}{\partial \theta} \sin \theta_i \Pi_\theta \right] + \omega^2 \mu \varepsilon \Pi_\theta \quad (4.17)$$

$$E_r = \frac{\partial}{\partial r} \left[\frac{1}{r^2} \frac{\partial}{\partial r} (r^2 \Pi_r) + \frac{1}{r \sin \theta_i} \frac{\partial}{\partial \theta} \sin \theta_i \Pi_\theta \right] + \omega^2 \mu \varepsilon \Pi_r \quad (4.18)$$

Using the expression given for Π_z and the spherical coordinate transformation

$$E_\theta = \frac{I(\omega)h}{j\omega\varepsilon} \left[\frac{1}{r} \frac{\partial}{\partial r} + \omega^2 \mu \varepsilon \right] \Pi \sin \theta_i \quad (4.19)$$

$$E_r = -\frac{I(\omega)h}{j\omega\varepsilon} \left[\frac{\partial^2}{\partial r^2} + \omega^2 \mu \varepsilon \right] \Pi \cos \theta_i \quad (4.20)$$

Replacing $\frac{\partial}{\partial r}$ with $j\omega\sqrt{\varepsilon\mu} \frac{\partial}{\partial(jk_0r)}$, and ω^2 with $-(j\omega)^2$, expressions for electric fields become

$$E_\theta = \frac{I(\omega)h}{\varepsilon} \left[\frac{\sqrt{\varepsilon\mu}}{r} \frac{\partial}{\partial(jk_0r)} - j\omega\mu\varepsilon \right] \Pi \sin \theta_i \quad (4.21)$$

$$E_r = -\mu I(\omega) h j \omega \left[\frac{\partial}{\partial (jk_0 r)^2} - 1 \right] \Pi \cos \theta_i \quad (4.22)$$

In the far-field the dominant terms in the aforementioned expressions are

$$E_\theta \approx -j \omega \mu I(\omega) h \Pi \sin \theta_i \quad (4.23)$$

$$E_r \approx j \omega \mu I(\omega) h \Pi \cos \theta_i \quad (4.24)$$

4.4 Implementation of the Model

The block diagram of the process of modulating, sending, and recovering UWB signal is shown in Figure 4.3. Given the binary sequence, binary signal is modulated using PPM, and signal is transmitted as monocycle Gaussian waveform. The received signal is comprised of the transmitted and reflected waveforms and added noise, $n(t)$. In our case we can assume that additive noise is Gaussian distributed. The variance of the noise will govern the degree of ensemble averaging required to correctly recover the transmitted symbol. During the propagation of the signal through the channel, the signal is convolved with the impulse response of the channel, $h(t)$.

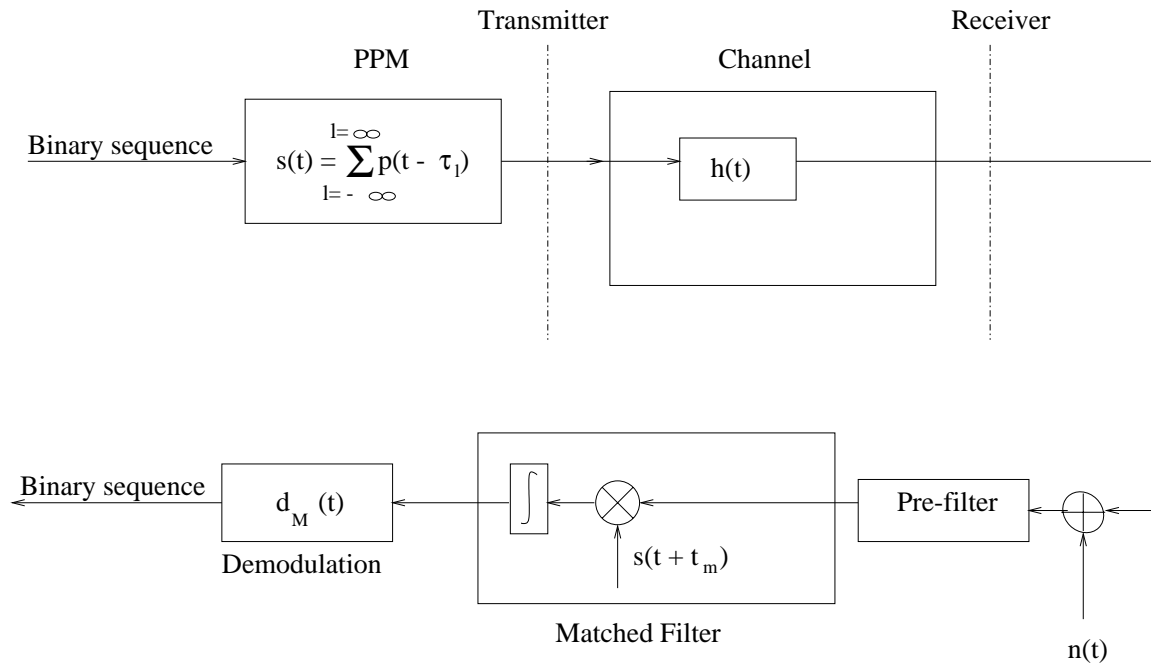


Figure 4.3. Block diagram of receiver and transmitter

When the signal reaches the receiver, the signal is put through filters. The function of the pre-filter is to equalize the response of the channel. To recover a single pulse under ideal conditions an stable inverse filter can be applied. However, in a real situation where thousands of pulses are transmitted to the receiver along different paths, the impulse response may not be minimum phase. For a non-minimum phase channel response the realization of inverse pre-filter for the channel is not possible. However, in this thesis we will not explore for solution of the optimal pre-filter.

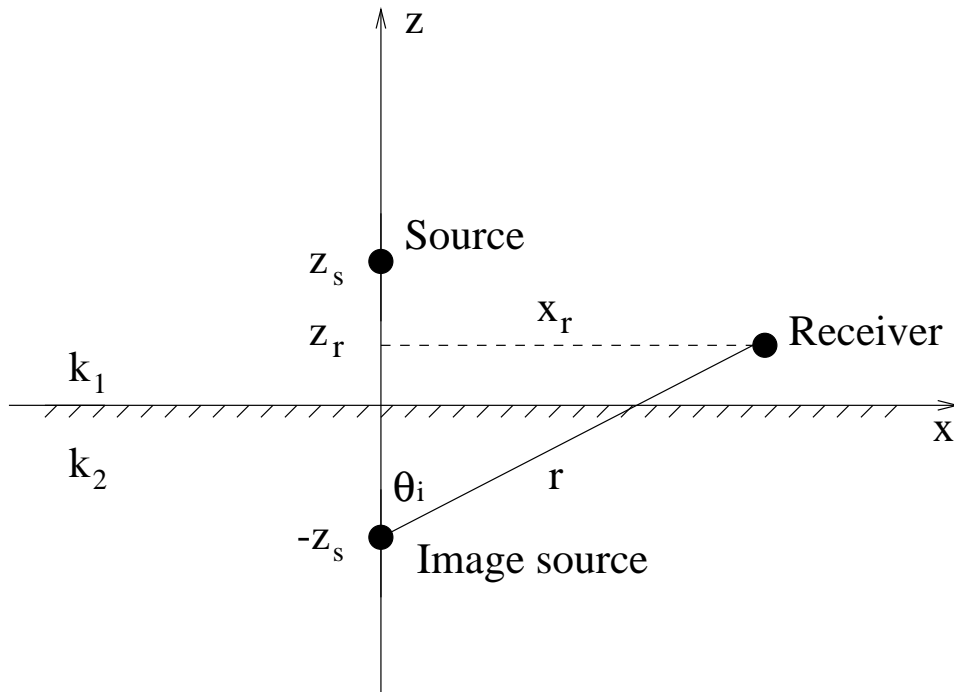


Figure 4.4. Position of the source and receiver

After the signal is pre-filtered, a matched filter is applied. At this point signal still contains noise. Hence, the matched filter will help to reduce noise effects in the determination of the time shift assigned to each received pulse. Knowing the exact shift of each pulse allows us to recover PPM signal. The recovered PPM signal can be demodulated with the pre-determined correlator yielding $d_M(t)$. Based on determined pulse-shifts demodulator decodes the PPM signal into the binary sequence.

In order to observe the influence of the single reflection on the UWB pulse the scenario shown in Figure 4.4 is assumed. In this case, the source is located at

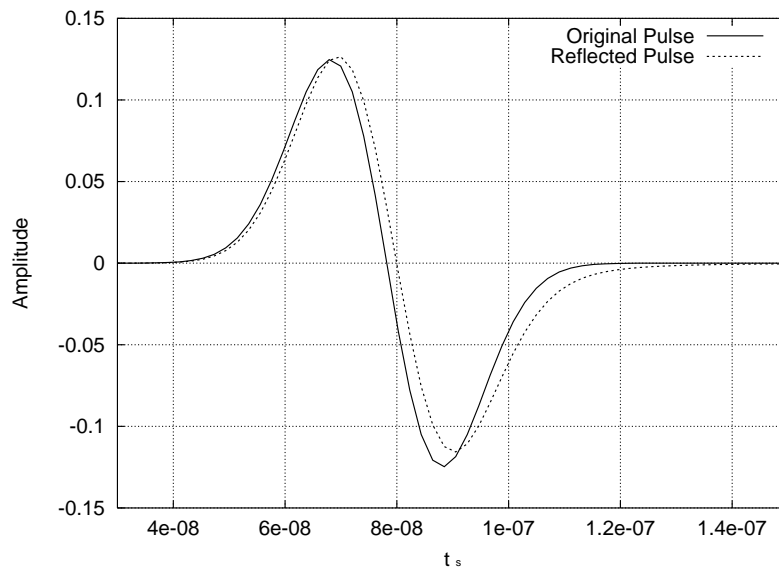
$(x, z) = (0, z_s)$, receiver at $(x, z) = (x_r, z_r)$. Distance between image source and receiver is defined as distance r . For the given scenario to be explored, the assigned position for the source is at $(x, z) = (0, 3m)$, and the receiver is at $(x, z) = (x_r, 1m)$. Position of the receiver is changed by adjusting the distance x_r . In this manner we can observe the pulse reflection at different distances and angles, where both r and θ_i are calculated from the positions of the source and receiver

$$r^2 = \sqrt{x_r^2 + (z_s + z_r)^2} \quad (4.25)$$

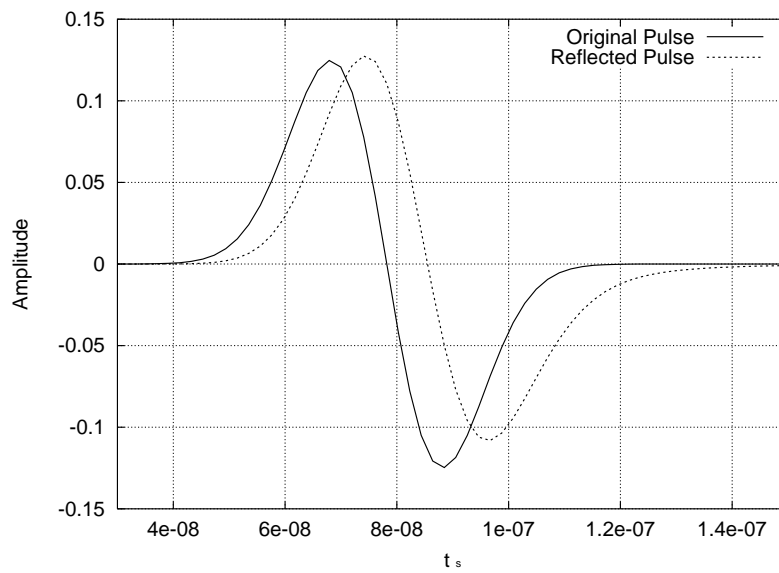
$$\theta_i = \sin^{-1} \left(\frac{x_r}{r} \right) \quad (4.26)$$

With finite height of the source ($z_s > 0$) for points of observation in medium 1 the angle has the finite range $0 \leq \theta_i < \frac{\pi}{2}$.

Calculated impulse response can be used to minimize the effect of any additional delays and pulse overlaps that occur due to the reflections during the transmission of the pulse train. Figure 4.5 is a time-domain comparison of a single pulse of PPM and the same pulse after it was convolved with the impulse response of the reflected field. PPM pulse was generated using previously defined parameters in Chapter 2.



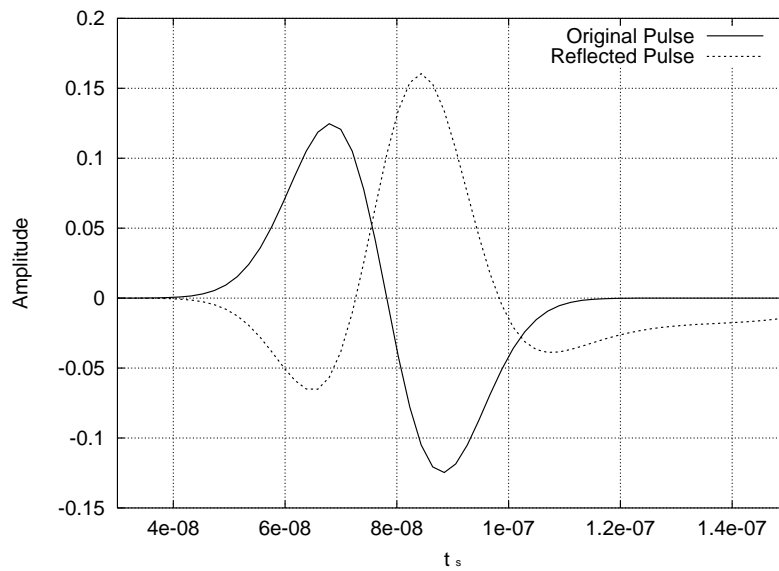
(a)



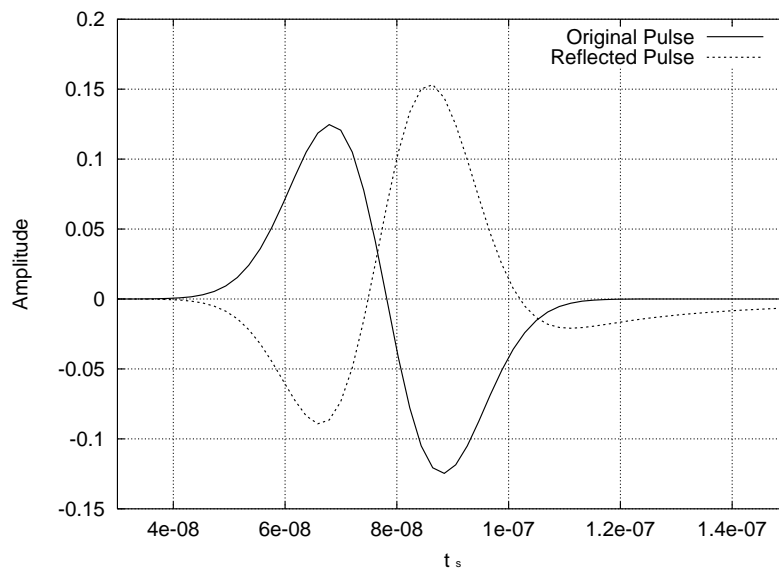
(b)

Figure 4.5. Reflected pulse for $\varepsilon = 3$ (a) $x_r = 1m$, $\tilde{r} = 6.67$, $\theta_i = 0.24rad$, (b)

$$x_r = 10m, \tilde{r} = 17.45, \theta_i = 1.19rad$$



(a)



(b)

Figure 4.6. Reflected pulse for $\varepsilon = 3$ (a) $x_r = 50m$, $\tilde{r} = 81.25$, $\theta_i = 1.49rad$, (b)

$$x_r = 100m, \tilde{r} = 162.12, \theta_i = 1.53rad$$

Convolution was done in the frequency domain, and result is obtained by taking the inverse of the Fourier transform with the previously described method. It can be seen that the short-range reflection has a strong impact on the pulse shape and the position within a time frame, both of which can be potential cause for the pulse interference. The time shift of r/c_1 and the amplitude reduction caused by spherical spreading is not considered. This choice will allow one to directly compare the the incident and reflected waveforms more easily.

Figure 4.5 represents the pulse reflection when the receiver is at distances 1m and 10m. Compared to the original pulse, in both cases the reflected pulses are shifted in the positive time-direction. However, Figure 4.6 demonstrate reflected pulses when the receiver is located at 50m and 100m. Both pulses are out of phase compared to the original pulse. Also, compared to the original pulse, the reflected pulses engage different shape. Time-shift caused by the single reflection of the pulse is proportional to the distance of the receiver from the image source.

Chapter 5

CONCLUSIONS

This thesis presented the solution for a single short-range reflection of UWB pulse using an image-based method based on Laplace-transform formulation of the Sommerfeld half-space problem. The improvement to the originally proposed problem is a more simple solution of the field. The complete field was calculated by evaluating a simple branch integral consisted in the reflection coefficient.

Chapter 2 described basic principles of modulation and demodulation that can be used in UWB. In order to shape energy spectrum and minimize interference with narrow band radio transmission, modulation technique of PPM was chosen. Demodulation was done in two stages: signal cancellation and signal demodulation. UWB pulse recovery in the presence of additive noise was achieved by using the matched filter, which maximizes the ratio of the output response to the input signal. The final stage of demodulation was achieved using a bit duration correlator.

The advantage of PPM is the usage of the random time-hopping code. In this kind of modulation, monocycles are less likely to overlap and interfere with each other. It was shown that, in the modulation, by adjusting the pulse width one could change the position of spectral nulls, and therefore, guard a particular frequency

and minimize the interference of the UWB signal.

Affective demodulation can be achieved only if both the transmitter and the receiver are synchronized and that they use the same random number generator. Matched filter was designed in such manner that its impulse response was equal to the conjugate of PPM signal. More accurate recovery of UWB pulse was achieved when averaged out over many realizations.

In Chapter 3, the reflection of a spherical wave generated by a dipole antenna was evaluated from a planar surface. Given that the electric field and the magnetic field are continuous across the boundary of two mediums, the boundary was substituted with a point source. The corresponding image source had the same characteristics as the point source including its singularities. Since the poles and zeroes of the reflection coefficient cancel out, the only contribution from the singularities to the image source is provided by branch points. The solution of reflection coefficient therefore consisted of a simple branch integral which converged and could be easily evaluated numerically.

For very high frequencies and large distance between a source and the receiver plane, wave reflection was a good approximation for a spherical wave reflection. The field around the dipole antenna showed a high degree of dependence on the values of the wavenumber, the distance between the image source and the

receiver, and the relative electric permittivity. Error was inversely proportional to the $k_1 r$ value. Furthermore, error decreased faster for the smaller values of ε . The signal was more likely to reflect at high amplitudes, low frequencies, and short distances.

The calculations of the complete field were done in the frequency domain. In Chapter 4, recovery of the UWB pulse using inverse FFT was shown. Also, we demonstrated the calculation methods for calculating the field impulse response using the Fast Fourier Transform algorithm. Without predicting the impulse response of a short-range reflection, the UWB pulse might be demodulated erroneously. In addition, the time-shift and the shape of the pulse were found to depend on the distance between the source and the receiver. For the shorter distances, pulses acquired an additional shift, and for the larger distances both the shape and the phase of the pulse changed.

Appendix A

DETAILED DERIVATION OF THE ENTIRE FIELD

Parallel-polarized reflection coefficient derived in Chapter 3 (Eqn (3.38)) is in the following form

$$\Gamma_{\parallel}(q) = \frac{\varepsilon q - \sqrt{1 + q^2}}{\varepsilon q + \sqrt{1 + q^2}} \quad (\text{A.1})$$

Due to the rational fraction, $\lim_{q \rightarrow \infty} \Gamma_{\parallel}(q)$ is subtracted from the original expression.

Detailed simplification of the mentioned step is given below

$$\begin{aligned} R(q) &= \Gamma_{\parallel}(q) - \lim_{q \rightarrow \infty} \Gamma_{\parallel}(q) \\ &= \frac{\varepsilon q - \sqrt{1 + q^2}}{\varepsilon q + \sqrt{1 + q^2}} - \frac{\varepsilon - 1}{\varepsilon + 1} \\ R(q) &= \frac{(\varepsilon + 1)(\varepsilon q - \sqrt{1 + q^2}) - (\varepsilon - 1)(\varepsilon q + \sqrt{q^2 + 1})}{(\varepsilon q + \sqrt{1 + q^2})(\varepsilon + 1)} \end{aligned} \quad (\text{A.2})$$

$$\begin{aligned}
&= \frac{\varepsilon^2 q - \varepsilon\sqrt{1+q^2} + \varepsilon q - \sqrt{1+q^2} - \varepsilon^2 q - \varepsilon\sqrt{1+q^2} + \varepsilon q + \sqrt{1+q^2}}{\left(\sqrt{1+q^2} + \varepsilon q\right)(\varepsilon + 1)} \\
&= \frac{2\varepsilon}{\varepsilon + 1} \frac{q - \sqrt{1+q^2}}{\varepsilon q + \sqrt{1+q^2}} \frac{\varepsilon q - \sqrt{1+q^2}}{\varepsilon q - \sqrt{1+q^2}} \\
&= \frac{2\varepsilon}{\varepsilon + 1} \frac{q^2 + 1 - q\sqrt{1+q^2} - \varepsilon q\sqrt{1+q^2} + \varepsilon q^2}{(\varepsilon q)^2 - 1 - q^2} \\
&= \frac{2\varepsilon}{\varepsilon + 1} \frac{q^2(\varepsilon + 1) - q\sqrt{1+q^2}(\varepsilon + 1) + 1}{q^2(\varepsilon^2 - 1) - 1} \\
&= \frac{2\varepsilon}{(\varepsilon + 1)(\varepsilon^2 - 1)} \frac{(\varepsilon + 1) \left[q^2 - q\sqrt{1+q^2} + \frac{1}{\varepsilon + 1} \right]}{q^2 - \frac{1}{\varepsilon^2 - 1}} \\
&= \frac{\varepsilon}{\varepsilon^2 - 1} \frac{\left[q - \sqrt{1+q^2} \right]^2 + \frac{1 - \varepsilon}{1 + \varepsilon}}{q^2 - \frac{1}{1 - \varepsilon^2}} \tag{A.3}
\end{aligned}$$

Removal of $\lim_{q \rightarrow \infty} \Gamma_{\parallel}(q)$, provided easier observation of behavior of singularities.

Combination of Eqns (A.3) and (A.2) results with the expression

$$\Gamma_{\parallel}(q) = \frac{\varepsilon - 1}{\varepsilon + 1} + \frac{\varepsilon}{\varepsilon^2 - 1} \frac{\left[q - \sqrt{1 + q^2} \right]^2 + \frac{1 - \varepsilon}{1 + \varepsilon}}{q^2 - \frac{1}{1 - \varepsilon^2}} \quad (\text{A.4})$$

Parallel-polarized reflection coefficient can be expressed in terms of Laplace transform as

$$\Gamma_{\parallel}(q) = \int_0^{\infty} S_{\parallel}(p) e^{-pq} dp \quad (\text{A.5})$$

where $S_{\parallel}(p)$ is to be determined. Therefore, the inverse Laplace transform of the same is expressed as

$$S_{\parallel}(p) = \frac{1}{2\pi j} \int_{-j\infty+c}^{j\infty+c} \Gamma_{\parallel}(q) e^{qp} dq \quad (\text{A.6})$$

$$S_{\parallel}(p) = \frac{1}{2\pi j} \int_{-j\infty+c}^{j\infty+c} \left[\lim_{q \rightarrow \infty} \Gamma_{\parallel}(q) + R(q) \right] e^{qp} dp \quad (\text{A.7})$$

The integral of $\lim_{q \rightarrow \infty} \Gamma_{\parallel}(q)$ is an impulse function, which simplifies the integrator to

$$S_{\parallel}(p) = \frac{\varepsilon - 1}{\varepsilon + 1} \delta(p) + \frac{1}{2\pi j} \int_{-j\infty+c}^{j\infty+c} R(q) e^{qp} dp \quad (\text{A.8})$$

In Chapter 3 it was shown that the only singularities that influence behavior of the

integral are the branch points, and therefore, $S_{\parallel}(p)$ can be determined through the fairly simple branch integral

$$S_{\parallel}(p) = \frac{\varepsilon - 1}{\varepsilon + 1} \delta(p) + \frac{1}{2\pi j} \left[\int_{-j+\Delta}^{j+\Delta} F(q)e^{qp} dq + \int_{j-\Delta}^{-j-\Delta} F(q)e^{qp} dq \right] \quad (\text{A.9})$$

where,

$$F(q) = \frac{\varepsilon}{1 - \varepsilon^2} \frac{2q\sqrt{1 + q^2}}{q^2 - \frac{1}{\varepsilon^2 - 1}} \quad (\text{A.10})$$

In order to establish the expression that is convenient for numerical evaluations, the substitution, $q = jy$, is introduced

$$S_{\parallel}(p) = \frac{\varepsilon - 1}{\varepsilon + 1} \delta(p) + \frac{\varepsilon}{1 - \varepsilon^2} \frac{1}{2\pi j} \left[\int_{-1}^1 \frac{2jy\sqrt{1 - y^2}}{-y^2 - \frac{1}{\varepsilon^2 - 1}} e^{piy} j dy - \int_1^{-1} \frac{2jy\sqrt{1 - y^2}}{-y^2 - \frac{1}{\varepsilon^2 - 1}} e^{piy} idy \right] \quad (\text{A.11})$$

Detailed derivation of $S_{\parallel}(p)$ is given below

$$S_{\parallel}(p) = \frac{\varepsilon - 1}{\varepsilon + 1} \delta(p) + \frac{\varepsilon}{1 - \varepsilon^2} \frac{1}{2\pi j} \left[- \int_1^{-1} \frac{2y\sqrt{1-y^2}}{y^2 + \frac{1}{\varepsilon^2 - 1}} e^{pijy} dy - \int_1^{-1} \frac{2y\sqrt{1-y^2}}{-y^2 - \frac{1}{\varepsilon^2 - 1}} e^{pijy} dy \right] \quad (\text{A.12})$$

$$= \frac{\varepsilon - 1}{\varepsilon + 1} \delta(p) - \frac{2\varepsilon}{1 - \varepsilon^2} \frac{1}{\pi j} \int_1^{-1} \frac{y\sqrt{1-y^2}}{y^2 + \frac{1}{\varepsilon^2 - 1}} e^{pijy} dy$$

$$= \frac{\varepsilon - 1}{\varepsilon + 1} \delta(p) - \frac{2\varepsilon}{1 - \varepsilon^2} \frac{1}{\pi j} \left[\int_1^0 \frac{y\sqrt{1-y^2}}{y^2 + \frac{1}{\varepsilon^2 - 1}} e^{pijy} dy + \int_0^{-1} \frac{y\sqrt{1-y^2}}{y^2 + \frac{1}{\varepsilon^2 - 1}} e^{pijy} dy \right]$$

$$= \frac{\varepsilon - 1}{\varepsilon + 1} \delta(p) - \frac{2\varepsilon}{1 - \varepsilon^2} \frac{1}{\pi j} \left[- \int_0^1 \frac{y\sqrt{1-y^2}}{y^2 + \frac{1}{\varepsilon^2 - 1}} e^{pijy} dy + \int_0^{-1} \frac{y\sqrt{1-y^2}}{y^2 + \frac{1}{\varepsilon^2 - 1}} e^{pijy} dy \right]$$

$$= \frac{\varepsilon - 1}{\varepsilon + 1} \delta(p) - \frac{2\varepsilon}{1 - \varepsilon^2} \frac{1}{\pi j} \int_0^1 \frac{y\sqrt{1-y^2}}{y^2 + \frac{1}{\varepsilon^2 - 1}} \left(e^{-pijy} - e^{pijy} \right) dy$$

$$= \frac{\varepsilon - 1}{\varepsilon + 1} \delta(p) + \frac{\varepsilon}{1 - \varepsilon^2} \frac{4}{\pi} \int_0^1 \frac{y\sqrt{1-y^2}}{y^2 + \frac{1}{\varepsilon^2 - 1}} \sin(py) dy \quad (\text{A.13})$$

The total field is defined as

$$\Pi(r, k) = \int_0^{\infty} S_{||}(p) \frac{e^{ik_1\psi}}{\psi} dp \quad (\text{A.14})$$

A point source of diameter h is considered to be at the coordinate $(x, y, z) = (0, 0, z_s)$ (Figure 3.13). Therefore,

$$\psi = \sqrt{x^2 + y^2 + \left(z + z_s + \frac{jp}{k_1\sqrt{\mu\varepsilon - 1}}\right)^2} \quad (\text{A.15})$$

The distance from the image source to the receiver, r , is defined as

$$r = x^2 + y^2 + (z + z_s)^2 \quad (\text{A.16})$$

Previously used normalizing propagation factor, $q = \frac{\cos \theta_i}{\sqrt{\mu\varepsilon - 1}}$, is implemented back

into the ψ function

$$\psi = r \sqrt{1 + \frac{2jp}{rk_1} \frac{\cos \theta_i}{\sqrt{\mu\varepsilon - 1}} - \left(\frac{p}{rk_1\sqrt{\mu\varepsilon - 1}}\right)^2} \quad (\text{A.17})$$

Finally, implementing Eqn (A.17) into Eqn (A.14), the field expression is

$$\Pi(r, k) = \frac{e^{jk_1 r}}{r} \left[\int_0^\infty S_{\parallel}(p) \frac{e^{jk_1 r \left(\frac{\psi}{r} - 1\right)}}{\frac{\psi}{r}} dp \right] \quad (\text{A.18})$$

REFERENCES

1. Hertz, H.R., "Electric Waves, Being Researches on the Propagation of Electric Action with Finite Velocity Through Space," Dover Publications, New York, 1962.
2. De Rosa, L.A., "Timing System," U.S. Patent 2,438,904, April 6, 1948.
3. De Rosa, L.A., "Random Impulse System," U.S. Patent 2,671,896, March 9, 1954.
4. Hoepfner, C.H., "Pulse Communication System," U.S. Patent 2,999,128, September 5, 1961.
5. Ross, G.F., "The Transient Analysis of Multiple Beam Feed Networks for Array Systems," PhD dissertation, Polytechnic Institute of Brooklyn, Brooklyn, NY, 1963.
6. Ross, G.F., "The Transient Analysis of Certain TEM Mode Four-Port Networks," IEEE Trans. Microwave Theory and Tech., vol. MTT-14, No. 11, pp. 528-547, 1966.
7. Ross, G.F., "Pulse Generator," U.S. Patent 3,402,370, September 17, 1968.
8. Ross, G.F., "Transmission of Reception System for Generating and Receiving Base-Band Duration Pulse Signals Without Distortion for Short Base-Band Pulse Communication System," U.S. Patent 3,728,632, April 17, 1973.
9. Harmuth, H.F., "A Generalized Concept of Frequency and Some Applications," IEEE Transactions of Information Theory, vol. IT-14, No.3, May, 1968
10. Harmuth, H.F., "Application of Walsh Function in Communications," IEEE Spectrum, 1969.
11. Harmuth, H.F., "Interference Caused by Additional Radio Channels Using Nonsinusoidal Carriers," Second Symposium and Technical Exhibition on Electromagnetic Compatibility, Montreux, June 28-30, 1977.
12. Harmuth, H.F., "Frequency-Sharing and Spread-Spectrum Transmission with Large Relative Bandwidth," IEEE Transaction on Electromagnetic Compatibility, vol. EMC-20, No.1, February, 1978.
13. "Specifications of the Bluetooth System," Version 1.1, Promoter Members of Bluetooth SIG, Inc., February 2001.
14. Federal Communication Commission, "Revision of Part 15 of Commission's Rules Regarding Ultra-Wideband Transmission Systems," FCC 02-48, ET Docket 98-153, April 22, 2002.
15. Federal Communications Commission, "FCC Affirms Rules to Authorize the Deployment of Ultra-Wideband Technology," February 13, 2003.
16. Sommerfeld, A.N., "Propagation of Waves in Wireless Telegraphy," Ann. Phys. (Paris), vol.28, p665-736, 1909.
17. Tesla, N., "My Inventions," Barnes and Noble Books Inc, 1995.
18. Rolf, B., "Graphs to Prof. Sommerfeld's Attenuation Formula for Radio Propagation," Proc. IRE, vol. 18, pp 391-402, 1930.

19. Banos, A., "Dipole Radiation in the Presence of a Conducting Half-Space," Pergamon Press, London, 1966.
20. Burrows, C.R., "The Surface Waves in Radio Propagation Over Plane Earth, Proceeding of the IRE," vol. 25, no. 2, p219-228, February, 1937.
21. Epstein, P.S., "Radio Wave-Propagation and Electromagnetic Surface Waves," Proc. Nat. Acad. Sci., vol. 33, 195-199, 1947.
22. Bouwkamp, C.J., "Review of Epstein," P.S., Proc. Nat. Acad. Sci, vol. 33, pp 195-199, 1948.
23. Ott, H., "Die Sattelpunktmethode in der Umgebung eines Pols mit Anwendungen auf die Wellenoptik und Akustik," Ann. Physik 43, 393-404, 1943.
24. Banos, Jr. A., Wesley, J.P., "The Horizontal Electric Dipole in a Conducting Half-Space," Univ. Calif. Marine Physical Laboratory, SIO Reference 53-33, 1953.
25. Lindell, V., and Alanen, A., "Exact Image Theory for the Sommerfeld Half-Space Problem, part I: Vertical Magnetic Dipole," IEEE Trans. on Ant. and Prop., vol. 32, no. 8, August, 1984.
26. Lindell, V., and Alanen, A., "Exact Image Theory for the Sommerfeld Half-Space Problem, part I: Vertical Magnetic Dipole," IEEE Trans. on Ant. and Prop., vol. 32, no. 8, August, 1984.
27. Di, X., and Gilbert, K. E., "An Exact Laplace Transform Formulation for a Point Source Above a Ground Surface," J. Acoust. Soc. Am, vol. 93, (2), February, 1993.
28. Vitebskiy, S., Carin, L., Ressler, M. A., and Le, F. H., "Ultra-Wideband, Short-Pulse Ground-Penetrating Radar: Simulation and Measurement," IEEE Transactions on Geoscience and Remote Sensing, vol. 35, no. 3, May, 1997.
29. Cotton, M. G., Kuester, E. F., and Holloway, C. L., "A Frequency- and Time-Domain Investigation into the Geometric Optics Approximation for Wireless Indoor Applications," U.S. Department of Commerce, NTIA Report 00-379, June, 2000.
30. Stremmer, F. G., "Introduction to Communication Systems," 2nd edition, Addison-Wesley Publishing Company, 1982.
31. Harmuth, H.F., "Nonsinusoidal Waves for Radar and Radio Communication," New York: Academic Press, 1981.

BIOGRAPHY

Miroslava Raspopovic was born on November 8th, 1978 in Belgrade, Serbia. She attended University of Massachusetts Lowell, where she earned both her Bachelor of Science Degree in Electrical and Computer Engineering in 2001 and Master of Science Degree in Electrical Engineering in 2003. She worked on a number of research projects at the Center for Advanced Computation and Telecommunications.

Miroslava is currently interested in the wireless communications area. She earned many awards and honors, some of which include the Chancellors Medal, the Academic All-American award, and the Professor Carl A. Stevens Award for High Academic Achievements. She is also an associate member of Sigma Xi Scientific Research Society, Tau Beta Pi Engineering Honor Society, and Eta Kappa Nu Electrical Engineering Society.